

Review

Anisotropic Mechanical Behaviors of Shale Rock and Their Relation to Hydraulic Fracturing in a Shale Reservoir: A Review

Peng-Fei Yin ¹ , Sheng-Qi Yang ^{2,3,*}  and Pathegama Gamage Ranjith ⁴ 

¹ State Key Laboratory of Intelligent Construction and Healthy Operation and Maintenance of Deep Underground Engineering, China University of Mining and Technology, Xuzhou 221116, China; yinpengfei@cumt.edu.cn

² School of Mechanics and Civil Engineering, China University of Mining and Technology, Xuzhou 221116, China

³ Key Laboratory of Rock Mechanics and Geohazards of Zhejiang Province, School of Civil Engineering, Shaoxing University, Shaoxing 312000, China

⁴ Deep Earth Energy Research Laboratory, Department of Civil Engineering, Monash University, Melbourne, VIC 3800, Australia; ranjith.pg@monash.edu

* Correspondence: yangsqi@hotmail.com; Tel.: +86-516-83995856; Fax: +86-516-83995678

Abstract: Shale gas is an important supplement to the supply of natural gas resources and plays an important role on the world's energy stage. The efficient implementation of hydraulic fracturing is the key issue in the exploration and exploitation of shale gas. The existence of bedding structure results in a distinct anisotropy of shale rock formation. The anisotropic behaviors of shale rock have important impacts on wellbore stability, hydraulic fracture propagation, and the formation of complex fracture networks. This paper briefly reviews previous work on the anisotropic mechanical properties of shale rock and their relation to hydraulic fracturing in shale reservoirs. In this paper, the research status of work addressing the lithological characteristics of shale rock is summarized first, particularly work considering the mineral constituent, which determines its physical and mechanical behavior in essence. Then the anisotropic physical and mechanical properties of shale specimens, including ultrasonic anisotropy, mechanical behavior under uniaxial and triaxial compression tests, and tensile property under the Brazilian test, are summarized, and the state of the literature on fracture toughness anisotropy is discussed. The concerns of anisotropic mechanical behavior under laboratory tests are emphasized in this paper, particularly the evaluation of shale brittleness based on mechanical characteristics, which is discussed in detail. Finally, further concerns such as the effects of bedding plane on hydraulic fracturing failure strength, crack propagation, and failure pattern are also drawn out. This review study will provide a better understanding of current research findings on the anisotropic mechanical properties of shale rock, which can provide insight into the shale anisotropy related to the fracture propagation of hydraulic fracturing in shale reservoirs.

Keywords: shale; hydraulic fracturing; anisotropic mechanical behavior; fracture toughness; brittleness evaluation; fracability evaluation



Citation: Yin, P.-F.; Yang, S.-Q.; Ranjith, P.G. Anisotropic Mechanical Behaviors of Shale Rock and Their Relation to Hydraulic Fracturing in a Shale Reservoir: A Review. *Energies* **2024**, *17*, 1761. <https://doi.org/10.3390/en17071761>

Academic Editor: Hossein Hamidi

Received: 11 March 2024

Revised: 31 March 2024

Accepted: 1 April 2024

Published: 7 April 2024



Copyright: © 2024 by the authors. Licensee MDPI, Basel, Switzerland. This article is an open access article distributed under the terms and conditions of the Creative Commons Attribution (CC BY) license (<https://creativecommons.org/licenses/by/4.0/>).

1. Introduction

As a typical sedimentary rock, shale is widely distributed in the earth's crust. Shale gas has now become a strategically and globally significant unconventional resource [1,2]. Hydraulic fracturing is the core technology of shale gas development and is generally employed in the exploitation of shale gas [3–5]. The economic and efficient way for hydraulic fracturing to be performed is to create large-scale complex fracture networks, which is known as volume fracturing [6,7]. In addition, the effective implementation of hydraulic fracturing is closely related to the study of formation characteristics, including the in situ stress coefficient, strength and deformation properties of the rock, rock anisotropy and heterogeneity, distribution of natural fractures, and brittleness of the rock. Therefore, the

mechanical properties of shale are an important part of shale gas reservoir evaluation [8–10]. The mechanical properties of the rock matrix and bedding development, as well as the hardness and brittleness of the rock, can lead the borehole wall of shale gas to collapse, causing leakage, and other instability problems [11,12]. Understanding the anisotropic behaviors of shale rock has important impacts for shale energy exploration, wellbore stability, the interpretation of micro-seismic monitoring, etc. [13]. Shale has many fine pores and micro-cracks due to its fine mineral particles and structure. The developmental characteristics of these micro-pores and micro-cracks will have certain impacts on the mechanical characteristics of shale at the macro level. The analysis of the internal microstructure of shale specimens can provide some auxiliary reference value for the subsequent test analysis. Therefore, it is of practical significance to investigate the anisotropic mechanical properties of shale, for the purpose of better application to the hydraulic fracturing of the shale reservoir.

As a highly differentiated stratified rock, shale has strong anisotropy, and is generally considered a transversely isotropic material [14–17]. The anisotropy of shale rock can be mainly attributed to certain factors, such as mineral orientation [18–20], microcracks [21], stress state [22,23], and kerogen content [24]. Overall, it is important to conduct comprehensive research on the shale's characteristics while considering its heterogeneity and anisotropy [25]. Scholars have summarized the effects of various minerals on the mechanical characteristics of shale [26,27]. These studies show that clay and a TOC content of 30–40 wt% are critical for micro-structural deformation [28], ensuring the various flow properties [29] and elastic properties [30], and revealing that mineralogy controls the mechanical response of the rock matrix. Therefore, to evaluate a shale reservoir as to whether it is a good candidate for fracture stimulation, rock mineralogy analysis is necessary, and a result indicating high levels of quartz and a low clay content is quite positive [31].

Shale anisotropy plays a significant role in engineering activities, and weak beddings have important impacts for the initiation, propagation, and formation of the hydraulic fracture networks of shale [32]. In several different studies, a distinct anisotropy of shale rock has been proven to have had a distinct effect on mechanical behaviors under different stress conditions [25,27,32–37], as well as predominate in the initiation and propagation of hydraulic fractures [38–40]. Many previous experimental investigations have studied the mechanical behaviors of different clayey rocks. In the prior experimental investigations, the shale was processed in different bedding inclinations. Many laboratory-based mechanical tests on shale specimens from outcrops and reservoirs have been conducted, including compressive tests [32,41–43], tensile tests [44], three-point bending tests [45], direct shear tests [36,46], etc. These studies provided adequate data and grounds for comprehending the anisotropic mechanical properties of the shale specimens.

Brittleness plays a critical role in hydraulic fracturing design [47]. However, brittleness cannot be measured directly from seismic data, or well-log data, either [48]. Using the mineralogy and mechanical parameters, various brittleness indices have been developed to evaluate the fracability of shale formations. A brittleness index based on mechanical parameters may provide a more accurate result, as these parameters can reflect the influence of stress on the brittleness [2], since the brittleness changes as the shale-formation depth increases [49]. An index based on mineralogy has been widely employed in the oil and gas industry because the input parameters are easy to obtain; however, due to the high cost of well exploration, the required data are difficult to obtain [50]. The reliability of the brittleness evaluation of shale should be improved. However, many of the brittleness indices function mostly according to the assumptions of isotropy theories [51], and it is well known that the anisotropy of shale rock rises to a high degree, thus, the anisotropic properties should be considered in the brittleness evaluation.

Moreover, the previous tests on shale mechanics [52–54] show that the anisotropy of the fracture toughness of shale is high, and these results show scatter between different shales. During the shale fracturing, the beddings are usually weaker than the rock matrix, and this can easily lead to crack propagation, i.e., when the fracture meets a bedding plane it can either extend along it or penetrate across it [36]. It is established that when a hydraulic

fracture extends in the shale rock, it will be positively influenced by the bedding planes. The complex interaction between hydraulic fracture and bedding planes could be affected by several factors, i.e., the bedding strength, inclination, fluid injection rate, and so on. Compared to other discontinuities, bedding planes with large scales can be found more frequently in shale, particularly in continental stratum [55]. In general, the bedding planes have distinct effects on several aspects, including weakening the shear and tensile strength, disturbing fracture propagation, and complicating the interaction between the existing and induced fractures [56–60]. These results revealed that the stimulated fracture networks and the well extraction process are significantly affected by these discontinuities. Therefore, it is necessary to study the relationships between the bedding plane and the hydraulic fracture characteristics [61].

This paper briefly reviews previous work on the anisotropic mechanical properties of shale rock and their relation to hydraulic fracturing in shale reservoirs. The lithological characteristics of shale rock, particularly the mineral constituent, determine its physical and mechanical behavior in essence. In this paper, the status of the research addressing the lithological characteristics of shale rock is summarized first, and then the anisotropic physical and mechanical properties of shale specimens, including ultrasonic anisotropy, mechanical behavior under compression tests, and tensile property under the Brazilian test, as well as fracture toughness anisotropy in the literature, are summarized. The topics associated with anisotropic mechanical behavior under laboratory tests are addressed in this paper; in particular, the evaluation of shale brittleness based on its mechanical characteristics is discussed in detail. Finally, further concerns, such as the effects of the bedding on hydraulic fracturing failure strength, crack propagation, and failure pattern, are also drawn out. This review study will provide a better understanding of the current research findings on the anisotropic mechanical properties of shale rock, which might provide insight into the aspects of shale anisotropy related to hydraulic fracture propagation in shale reservoirs.

2. The Lithological Characteristics of Shale Rock

Rock mineralogy is essential for the evaluation of shale reservoirs [62,63], and can greatly determine the brittleness [47]. The anisotropy is induced by the packing density, which reveals that, in situ, the anisotropy of shale is from the deposition of the clay particles rather than from the intrinsic anisotropy of the mineral.

The mineral components of shale vary with different depositional and burial environments and aspects of its mineralogy [64]. The basic mineral components of shale rock are carbonates, quartz, clays, and feldspar. In many research works, the shales can be named according to the mineral enrichment, such as clay-rich shale [65–67], organic-rich shale [68–70], and carbonate-rich shale [71,72]. The relevant mineralogy plays an essential role in hydraulic fracturing implementation. Different proportions of quartz, carbonates, and clays could result in different mechanical properties in shale rocks. Shales with abundant quartz and a low clay content usually are of high brittleness, and shales that have a high clay content and low quartz content are low in brittleness [47,73].

As for the clay-rich shale, the common intrinsic clay minerals in petroleum reservoirs are kaolinite, chlorite, illite, smectite, and mixed-layer clays [74]. For instance, Pierre Shale [65], is a clay-rich rock, with its mineralogy dominated by mixed-layer illite–smectite, discrete illite, and quartz. Its microfabric shows a distinct amount of fine-grained rigid minerals floating in a clay matrix. This kind of shale is layered in places, with some high aspect-ratio rigid minerals, organic matter, and clays aligned sub-parallel to the bedding. Clay-rich shales have better reservoir properties, and they show higher porosity, pore volume, and specific surface. Clay-poor shales have higher concentrations of brittle minerals, resulting in limited shale gas storage, which makes the shale inadequate for shale gas exploration [66]. Organic-rich shales are usually considered to be good for petroleum and gas extraction [75]. The micro-pores are often developed at the nano-level in the organic-rich shale, leading to a prominent capillary effect and a high spontaneous

imbibition effect [69]. As for carbonate-rich shale, such as Mancos Shale [71], as shown in the XRF maps shown in Figure 1, the light band from the petrographic data indicates the quartz-calcite-rich laminae. It can be seen that Si is distributed in the matrix, while Ca, Al, Fe, K, and Mg are distributed between the optically lighter and darker layers. It also can be found that Al, K, Fe, and Mg are intensively distributed in the more fine-grained (optically darker) layers, and Ca is intensively distributed in the more coarse-grained (optically lighter) layers. The micro-texture of the quartz-calcite-rich laminae consists of isolated organic material and coarser-grained quartz, dolomite, and feldspar minerals, cemented by calcite.

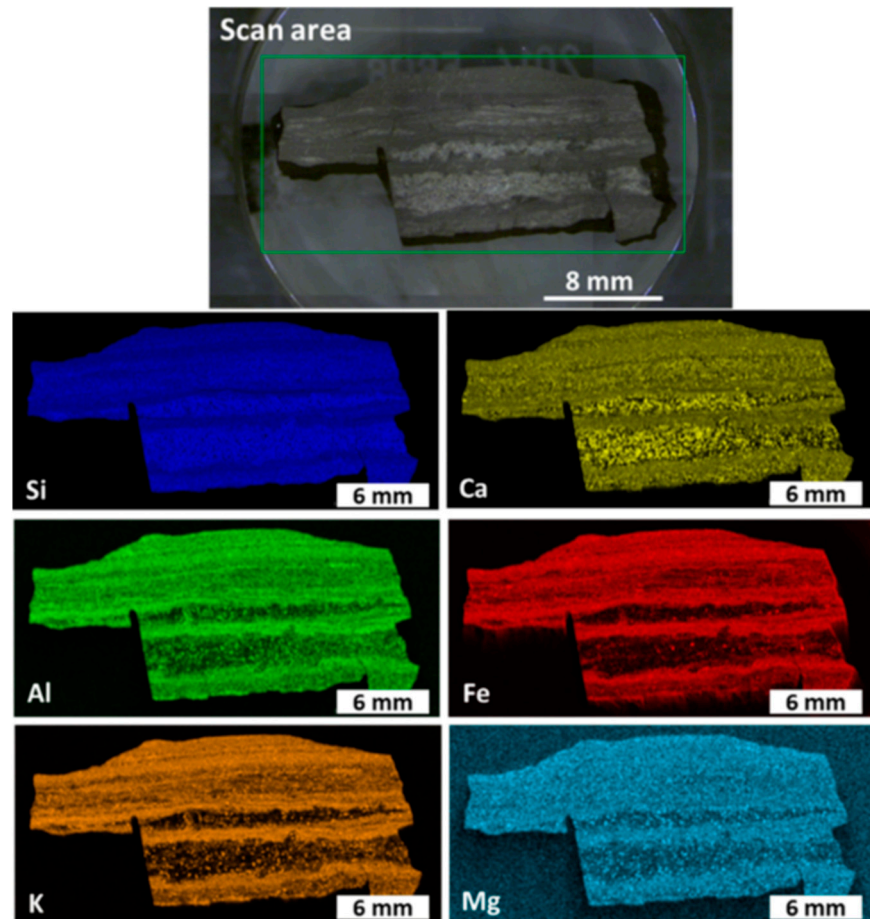


Figure 1. Micro-XRF maps for selected elements of Mancos Shale [71].

High quartz contents and low clay contents contribute to high levels of brittleness and help hydraulic fracture propagation. Li et al. [76] conducted research on black siliceous shale specimens from the southeastern edge of the Sichuan Basin of the Upper Yangtze Plate. The X-ray diffraction (XRD) results show that the brittle minerals of the shale specimen are 60–80 wt%, and that this gradually increases as the burial depth increases (Figure 2a). Figure 2b also shows that the clay content is low, and that the shale in the upper has clay-rich minerals, while the shale in the lower has brittleness-rich minerals like quartz [50].

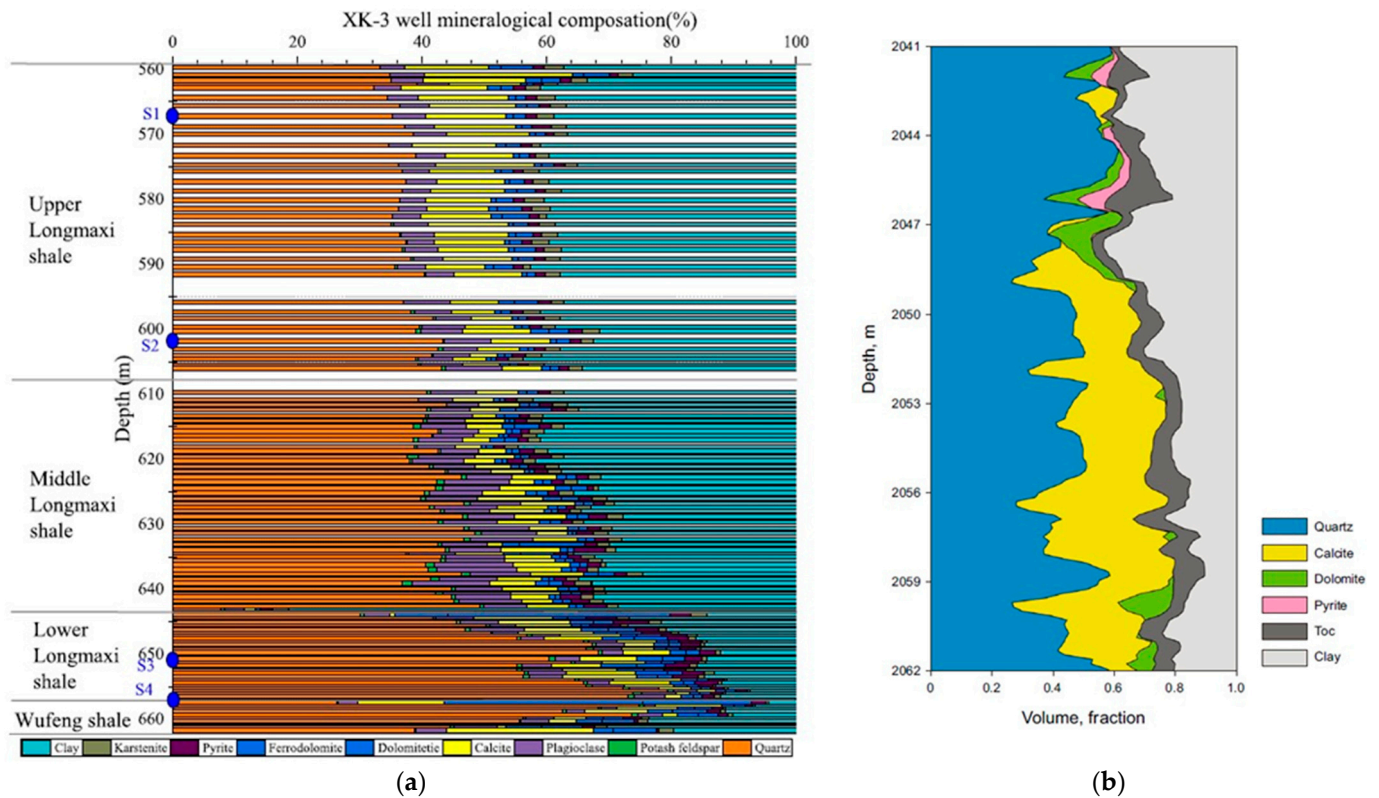


Figure 2. Mineral components of shale at different formation depths for the (a) shale of the Wufeng–Longmaxi Formation in well XK-3 [76]; (b) the mineralogy of target depths shows the volumetric fractions of constituents [50].

3. The Anisotropic Mechanical Behavior of Shale Specimens under Different Loading Conditions

The anisotropy should be carefully considered when attempting to predict the mechanical behaviors of shale [77]. Many research efforts have been conducted to study the mechanical behaviors of different rock materials containing high clay contents. As for those experiments, the shale specimen was processed in various loading directions relative to the bedding planes. In those studies, it was found that the anisotropic inclination of a shale specimen under a loading test is generally defined by two aspects: one is the angle of the loading line to the bedding plane [77–79], and the other one is the angle of the loading line relative to the normal direction of the bedding plane [11,25,80]. These two angles are complementary. To better compare and describe the test results of shale specimens in different studies, the anisotropic inclinations must be unified. As depicted in Figure 3, the angle θ of the loading line to the normal direction of the bedding plane is employed in this paper [2,11,81]. As illustrated in Figure 3a, the cylinder specimens with different bedding inclinations were loaded under the compression test, while, as seen in Figure 3b, the disc specimens were loaded under the Brazilian split test. Therefore, the anisotropic inclination θ is also the angle of the bedding plane relative to the horizontal line. The test data from different studies described in the following text are all standardized to this anisotropic inclination θ .

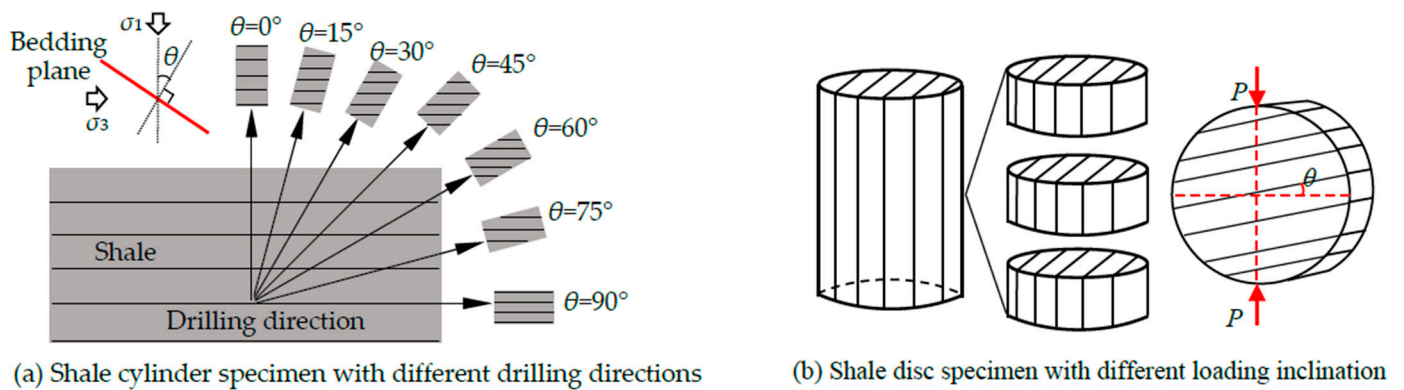


Figure 3. Preparation of shale specimens in different bedding inclinations.

3.1. Ultrasonic Anisotropy of Shale Specimens

Ultrasonic techniques are maneuverable and nondestructive, and therefore useful for applications in laboratory conditions, and are promising for geophysical applications, including the interpretation of the dynamic mechanical behaviors of shale [77]. The P-wave travels faster than the S-wave. The anisotropy affecting wave velocity in the shale subsurface is considered to be a central difficulty, one resulting in significant issues for understanding dynamic elasticity in geophysical interpretation. Elastic constants of geologic materials, such as shale reservoirs, can be determined by measuring wave velocities [82]. Lo et al. [83] conducted a series of tests on the wave velocities associated with Chicopee shale by using ultrasonic techniques. Their experimental results show that the mineral orientation and the micro pores or cracks are the main factors resulting in elastic anisotropy. Additionally, the elastic anisotropy decreases with increasing confining pressure. Allan et al. [84] investigated the anisotropy of wave velocity in an organic-rich shale by proposing a multiscale methodology as well as various analyses based on XRD tests, BSE-SEM tests, and X-ray microtomography, which were applied to determine and understand the sources of wave velocity anisotropy.

Based on some ultrasonic test data from shale specimens [77,85,86], Figure 4 depicts the relationships between ultrasonic velocities and bedding angles. It can be clearly seen that the ultrasonic velocities are obviously affected by the bedding planes, and that the velocities of P- and S-waves parallel to the bedding plane are greater than those of the waves orthogonal to the bedding plane. The energy decreases due to the wave scattering on different beddings, leading to increases in the time duration of the wave traveling through the specimens. The above conclusions are similar to the results from Dewhurst et al. [87] and Zhubayev et al. [88]. The experimental results from Mokhtari et al. [44] show that the P-wave velocity of a shale specimen with a bedding inclination of 0° is 30% lower than a specimen with a bedding inclination of 90° .

Based on the propagation and polarization directions relative to the bedding plane, six ultrasonic wave velocities can be measured in shale specimens [89]. Figure 5 illustrates the six velocities, as follows [90]: one compressional wave (V_{pv}) and two shear waves ($V_{sv1} = V_{sv2}$), which propagate normally to the bedding plane in a vertical plug (as shown in Figure 5a, $\theta = 0^\circ$); and one compressional wave (V_{ph}) and two shear waves ($V_{sh} > V_{sv}$), which propagate parallel to the bedding plane in a horizontal plug (as shown in Figure 5b, $\theta = 90^\circ$). These six ultrasonic velocity parameters could then be employed to calculate the elastic parameters, which are used for describing the anisotropic elastic properties of a vertically transverse isotropic (VTI) material like shale rock [91,92].

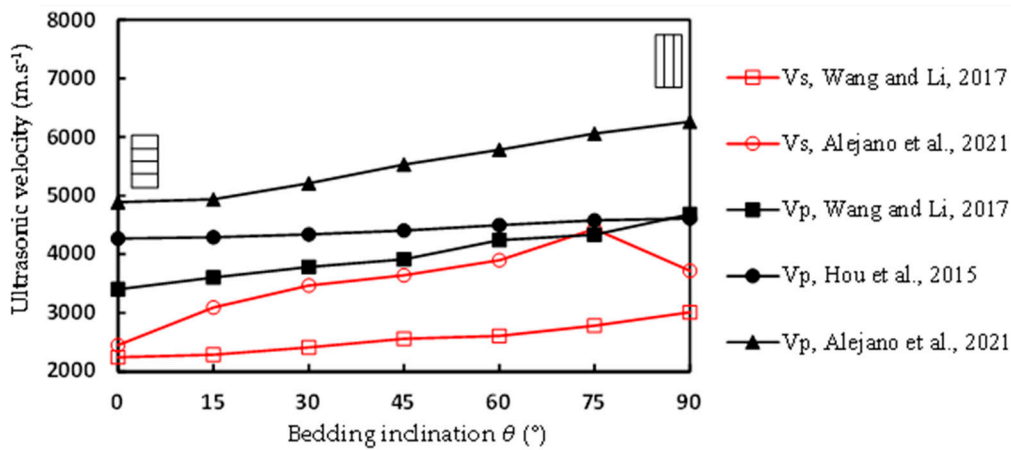


Figure 4. Ultrasonic velocity variation with respect to bedding inclination in shale specimens [77,85,86].

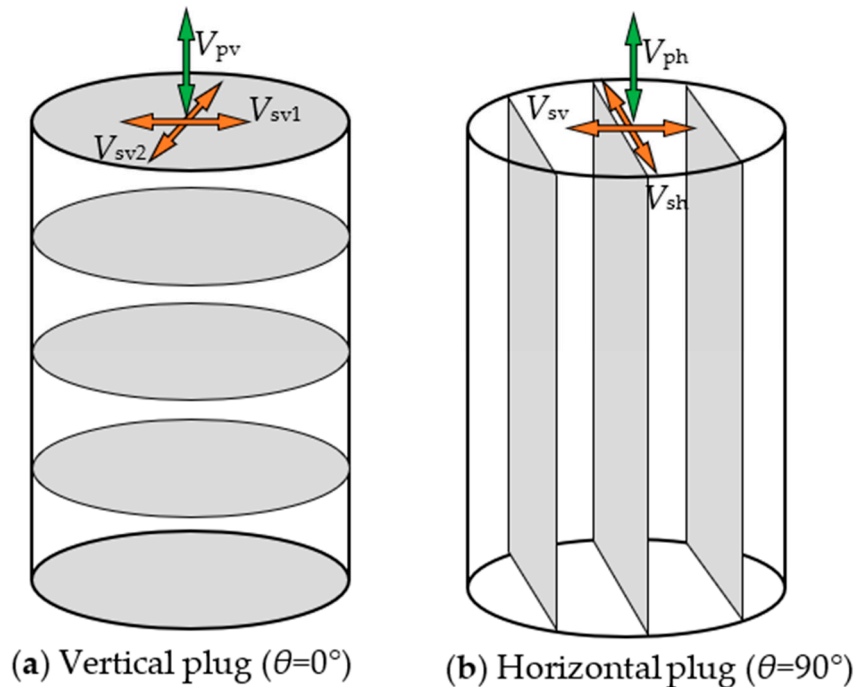


Figure 5. Schematic representation of wave velocity measurements commonly used in ultrasonic testing: (a) the wave travels normal to the bedding plane ($\theta = 0^\circ$); and (b) the wave travels parallel to the bedding plane ($\theta = 90^\circ$). (Adapted from Iferobia and Ahmad [90].)

In the study conducted by Yin [93], the wave’s attenuation by bedding planes in the transversely isotropic rock is also described. As depicted in Figure 6, when the ultrasonic wave travels normal to the bedding, the transmission and reflection occur synchronously at the bedding plane (Figure 6a), and the wave’s reflection results in energy loss and reduces the wave’s velocity; with more bedding planes orthogonal to the propagation direction, greater energy losses occur, leading to a lower velocity of the ultrasonic wave. At a bedding inclination of 0° (Figure 6a), the bedding planes are orthogonal to the propagation direction of the P-wave, resulting in strong reflection at the bedding planes and a lower wave-velocity. With the increases of bedding inclination, the beddings are slowly brought parallel to the propagation direction, and the energy attenuation becomes less, leading to an increase in wave velocity. When at a bedding inclination of 90° (Figure 6b), the bedding planes are parallel to the propagation direction of the P-wave, and there is almost no reflection and the energy attenuation is minimum; thus, the wave velocity is at its maximum.

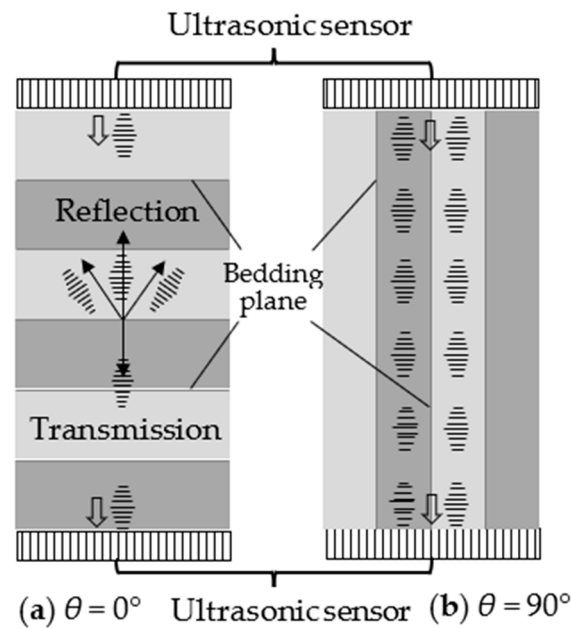


Figure 6. A schematic diagram of longitudinal wave propagation in transversely isotropic rock. (Adapted from Yin and Yang [93]).

3.2. Uniaxial and Triaxial Compression Test

Shale specimens with various bedding inclinations are frequently studied to investigate their anisotropic behaviors. Many researchers have conducted experiments on various shale specimens under compression conditions [36,41,42,46,78,94–104]. The above studies reported the mechanical properties of anisotropic rocks; in particular, in Ramamurthy's research [105], the anisotropy of rocks is generally classified into three modes: "U" type, undulatory type, and "shoulder" type. These are shown in Figure 7.

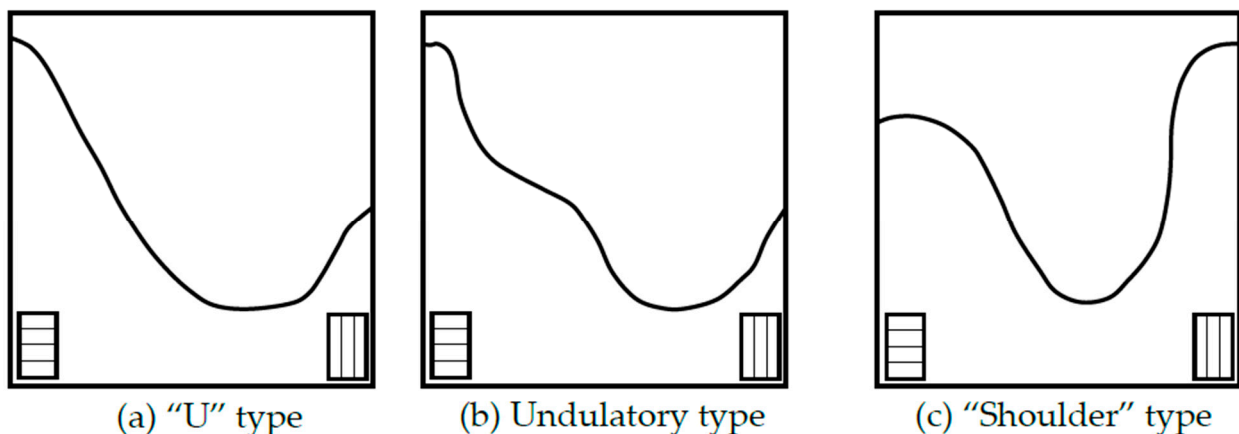


Figure 7. Three types of strength variation relative to the bedding inclination of the anisotropic rock.

Strength under triaxial compression conditions is the key characteristic of rock material. Some tests are conducted under uniaxial compression [2,11,25,36,77–80,85,86,95,106,107], and some tests are conducted under triaxial compression conditions [2,36,78,85,108]. The various shale specimens taken from different sampling sites in these studies display different magnitudes of strength, but their values all show a similar law of variation concerning the bedding inclination. Based on the test data from the above-mentioned studies, the uniaxial compressive strength (UCS) and triaxial compressive strength (TCS) variations with respect to bedding inclination are displayed in Figures 8 and 9, respectively. From Figures 8 and 9, it can be concluded that the peak strength instances all display a "U" type

or a similar “shoulder” type variation with increased bedding inclination under different confining pressures. Particularly, the maximum peak strength is observed at $\theta = 0^\circ$ or 90° , and the minimum values are observed at $45^\circ < \theta < 75^\circ$.

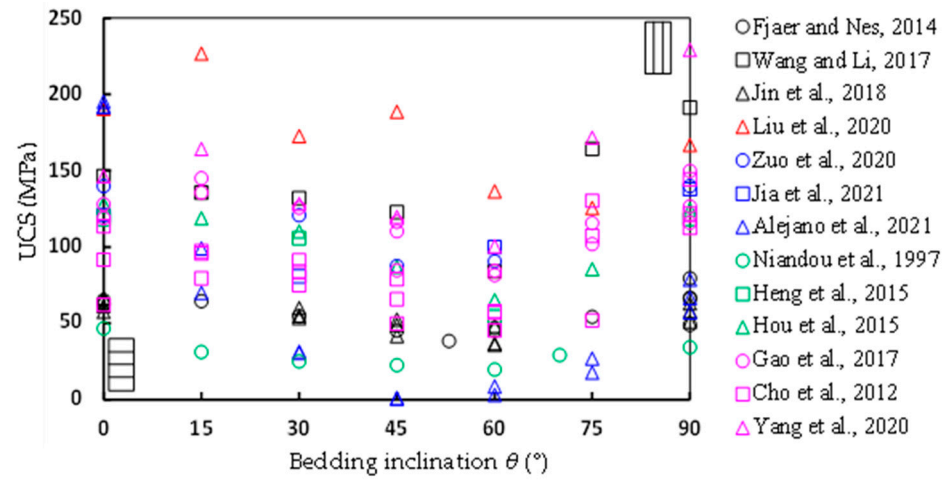


Figure 8. Uniaxial compressive strength (UCS) variation with respect to bedding inclination in shale specimens [2,11,25,36,77–80,85,86,95,106,107].

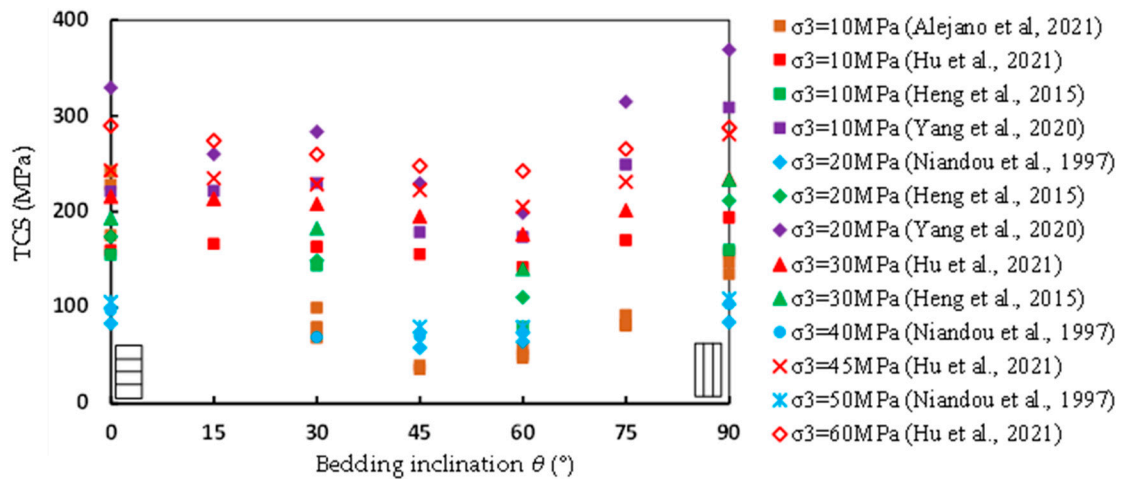


Figure 9. Triaxial compressive strength (TCS) variation with respect to the bedding inclination of shale specimens [2,36,78,85,108].

To better predict the strength of anisotropic rocks, many strength criteria have been proposed. The earliest attempt was the theory of a single weakness plane [109], and this was followed by various subsequent studies [110–117]; in one, an empirical strength criterion was proposed for predicting the non-linear strength behavior of intact anisotropic rocks [111,112]:

$$\frac{(\sigma_1 - \sigma_3)}{\sigma_3} = B_j \left(\frac{\sigma_{cj}}{\sigma_3} \right)^{\alpha_j} \quad (1)$$

where σ_1 and σ_3 are the major and minor principal stresses, respectively, and σ_{cj} is the UCS at the particular θ . The values for α_j and B_j are defined herein to consider the anisotropy of the strength, and the functions are as follows:

$$\frac{\alpha_j}{\alpha_{90}} = \left(\frac{\sigma_{cj}}{\sigma_{c90}} \right)^{1-\alpha_{90}} \quad (2)$$

$$\frac{B_j}{B_{90}} = \left(\frac{\alpha_{90}}{\alpha_j} \right)^{0.5} \quad (3)$$

where σ_{c90} is the UCS at $\theta = 90^\circ$, and α_{90} and B_{90} are the values of α_j and B_j at $\theta = 90^\circ$. The values for α_j and B_j at each anisotropy orientation can be calculated by substituting the triaxial compression test data into Equation (1). Additionally, another empirical criterion under triaxial conditions can be expressed as follows [118]:

$$\frac{\sigma_1}{\sigma_{ci}} = \frac{\sigma_3}{\sigma_{ci}} + \left[\frac{1 + A(\sigma_3/\sigma_{ci})}{1 + B(\sigma_3/\sigma_{ci})} \right] - r \quad (4)$$

where σ_{ci} is the UCS of intact rock; A and B are constant parameters; and r is the strength reduction factor, with a value equal to 0 for intact rock and 1 for highly jointed rock masses. To better apply the above failure criterion to transversely isotropic rocks, Saeidi et al. [114] modified the failure criterion (Equation (4)) to the following:

$$\sigma_1 = \sigma_3 + \sigma_{c\theta} \left[\frac{1 + A(\sigma_3/\sigma_{c\theta})}{\alpha + B(\sigma_3/\sigma_{c\theta})} \right] \quad (5)$$

where $\sigma_{c\theta}$ is the UCS of anisotropic rock at θ , and α is the strength reduction parameter when taking into account the anisotropy, which is considered here in order to extend the generalization of Equation (4) to anisotropic rocks.

In addition, several mechanical models based on a damage theory have been proposed for anisotropic rocks by a series of researchers [119–123]. These models show a good capability for describing the main mechanical behaviors of anisotropic rocks, but still need to be verified by more experimental data for different types of anisotropic rocks. To evaluate the effect of the confining pressure on anisotropy, the strength anisotropy degree R_a , represented in terms of $\sigma_{pmax}/\sigma_{pmin}$, can be calculated in each confining pressure [113,124]. The strength anisotropy degree R_a indicates the maximum degree of strength deviation under different bedding inclinations. Figure 10 shows the variations of R_a with increases in confining pressure, the data for which are calculated based on the studies in Figures 8 and 9. It can be seen that the strength anisotropy degree R_a of a shale specimen decreases as the confining pressure increases. In other words, the confining pressure can reduce the strength anisotropy of rock material. The reason is that the confining pressure is hydrostatic pressure, and when it is applied to the specimen, the beddings are compacted, and thus the bedding strength is enhanced, and the bedding effect is weakened.

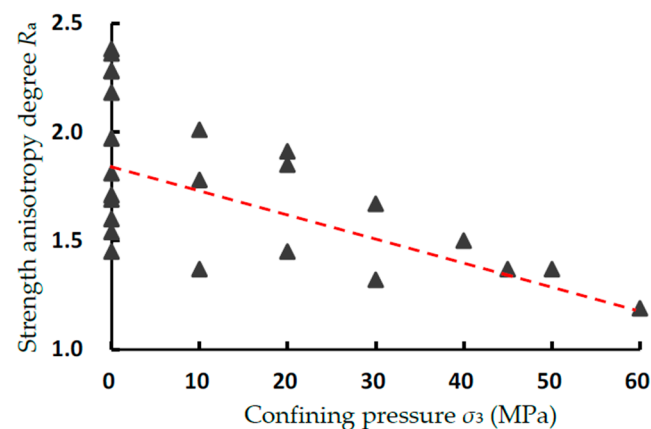


Figure 10. Strength anisotropy degree variation with respect to the bedding inclination of shale specimens.

In addition, Figure 11 shows the elastic modulus with bedding inclination increases under uniaxial compression of shale specimens, based on data drawn from some previous studies [11,25,36,77,80,86,106,107]. These studies all reported an increasing variation with the bedding inclination increases overall, even though there were some local fluctuations. The explanation for this can be developed as follows: (1) the directional alignment of the clay minerals and micro-cracks in the bedding plane is the inherent reason for the strong elastic anisotropy of the shale specimen [125], and the content of the clay and the development

of micro-cracks are different in the specimens under different bedding inclinations; this results in the anisotropy of the elastic modulus [86]; (2) as typical sedimentary rock, the compaction degree of the bedding in shale rock is low in the diagenetic process. Therefore, when the principal stress is parallel to the bedding ($\theta = 90^\circ$), the bedding is under a tensile state and the rock matrix is under compression; thus, the elastic modulus and deformation modulus are large and, this is in accord with the rock matrix in this case. When the principal stress is perpendicular to the bedding ($\theta = 0^\circ$), the bedding is in a state of compaction, and the axial strain is larger, resulting in a smaller elastic modulus and deformation modulus.

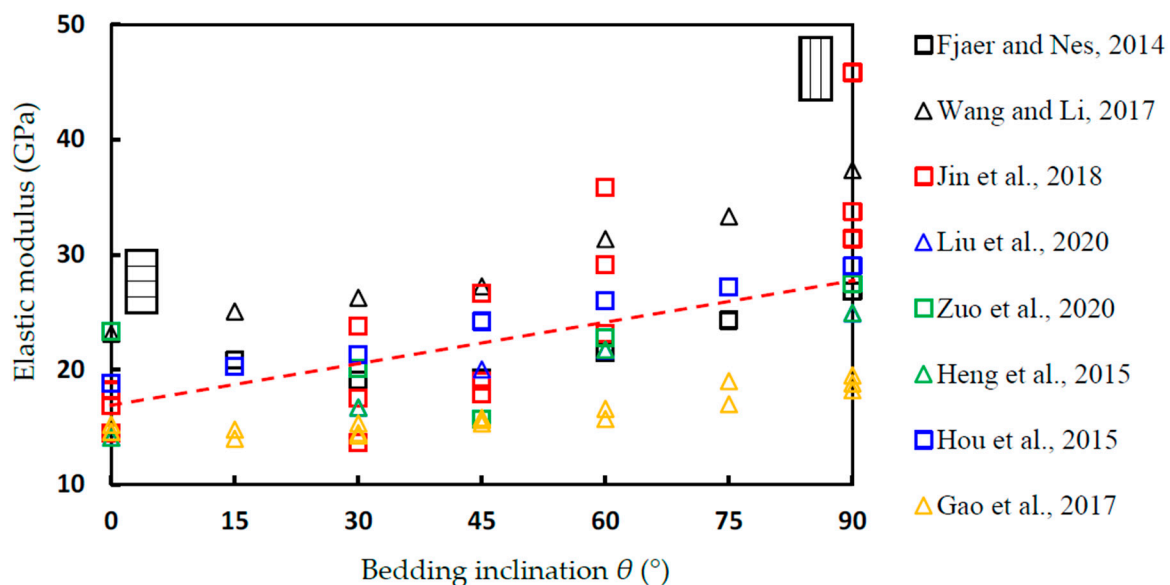


Figure 11. Elastic modulus with respect to inclination angle under uniaxial compression of shale specimens [11,25,36,77,80,86,106,107].

As for the failure behavior of shale rock under the conventional triaxial compression test, the fracture propagation during the failure process is generally affected by the bedding inclination and the confining pressure. The fracture angle strongly depends on the bedding inclination and the confining pressure. In the summary of Niandou et al. [78], for a bedding inclination of $0^\circ < \theta < 30^\circ$, tensile fracture along the loading direction occurs under low confining pressure and shear fracture across the bedding plane occurs under high confining pressure. For a bedding inclination of $30^\circ < \theta < 75^\circ$, the failure generally occurs by the bedding sliding; however, shear fracture in the matrix can occur and may cross the bedding plane when under a high confining pressure. For a bedding inclination of $75^\circ < \theta < 90^\circ$, when under low confining pressure, the failure occurs by the bedding plane splitting, and failure occurs by a shearing across the bedding plane when under a high confining pressure. In the study of Yang et al. [2], the researchers conducted conventional triaxial compression tests on Longmaxi Formation shale specimens under different bedding inclinations. According to the test results, they classified the shale specimens into four failure modes, as illustrated in Figure 12 and Table 1. Four failure modes are reported: tensile fracture through the bedding plane (T-T), tensile fracture along the bedding plane (T-A), shearing through the bedding plane (S-T), and shearing along the bedding plane (S-A). T-T generally occurs under uniaxial compression (or very low confining pressure) with low and medium bedding inclination (0° – 45°). S-A mainly takes place in specimens with medium or high bedding inclinations (45° – 75°). With increases in the confining pressure, S-T occurs in specimens with low or medium bedding inclinations (0° – 45°), instead of T-T, and even in some high bedding inclinations, the S-T dominates the failure. As for the bedding inclination of 90° , T-A occurs when under uniaxial compression, as the bedding is activated by tension along the loading direction. With the increases in confining increases, S-T takes place in the rock matrix. It can be concluded that the bedding planes at medium

and high inclinations have a distinct effect on the failure fracture, resulting in shear slipping along the bedding plane; with the increases in confining pressure, high confining pressure dominates the failure mode and shear fracture in the matrix (across the bedding plane) generally occurs, which is similar to the mode of isotropic rock material. These findings are also in accord with the studies of Liu et al. [80] and Zhao et al. [126].

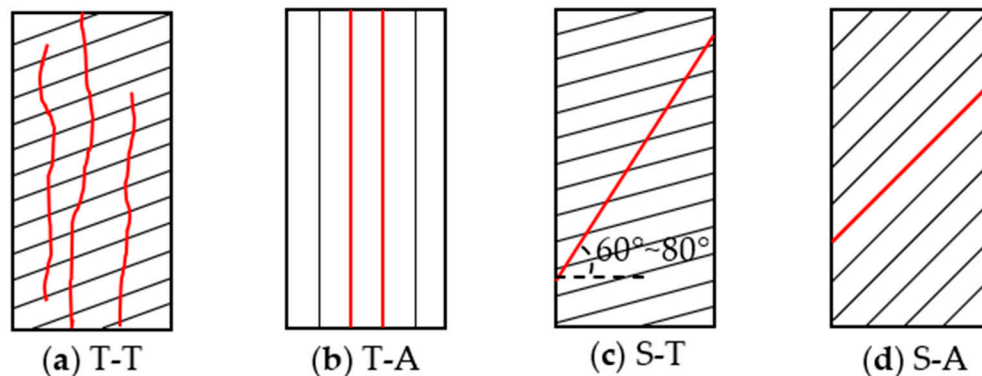


Figure 12. Classification of failure modes of shale specimens [2].

Table 1. Failure mode summary for shale specimens, from the study of Yang et al. [2].

	$\theta = 0^\circ$	$\theta = 15^\circ$	$\theta = 30^\circ$	$\theta = 45^\circ$	$\theta = 60^\circ$	$\theta = 75^\circ$	$\theta = 90^\circ$
$\sigma_3 = 0$ MPa	T-T	T-T	T-T	T-T	S-A	T-T	T-A
$\sigma_3 = 5$ MPa	S-T	S-T	S-T	S-A	S-A	S-A, S-T	S-T
$\sigma_3 = 10$ MPa	S-T	S-T	S-T	S-A, S-T	S-A	S-A, S-T	S-T
$\sigma_3 = 15$ MPa	S-T	S-T	S-T	S-A, S-T	S-A	S-A	S-T
$\sigma_3 = 20$ MPa	S-T	S-T	S-T	S-A, S-T	S-A	S-A	S-T

3.3. Tensile Properties under Brazilian Split Test

The tensile strength of shale plays an important role in the initiation and propagation of hydraulic fractures. As a method classically used to evaluate the tensile strength, the Brazilian test with different bedding inclinations is widely employed for determining structural anisotropy. The analytical solution developed to measure the tensile strength of anisotropic rocks was developed by Amadei et al. [127] according to the theoretical relation between the stress and strain proposed by Lekhnitskii et al. [128]. The effects of bedding inclination and thickness on tensile strength and the fracture pattern of anisotropic rocks under diametrical loading conditions have been investigated by conducting various Brazilian tests [15,129–134].

Vervoort et al. [133] summarized the failure anisotropy of nine different anisotropic rocks under Brazilian test conditions into four trends, as follows (as shown in Figure 13).

Trend 1: Constant value over the entire range of anisotropy angles (Figure 13a).

Trend 2: Constant value between 0° and 45° , followed by a linear decrease (Figure 13b).

Trend 3: Decrease in the strength over the entire interval, but a rather systematic decrease, approximating a linear variation (Figure 13c).

Trend 4: Decrease from very low anisotropy angles (between 0° and 30° – 40°), followed by a leveling off (Figure 13d).

The above four variation trends describe different types of anisotropic rocks with varying bedding planes. As for the shale rock specimens from different studies, the BTS variation with respect to bedding inclination is similar. Figure 14 summarizes some BTS data of shale specimens from different studies. From their test results, depicted in Figure 14, it can be seen that the BTS variation of shale specimens is more like the above trend 2 and trend 4. The studies of Jin et al. [25], Yang et al. [81], and Cho et al. [95] show that the BTS value is constant between 0° and 60° and then followed by a linear decrease, which is in accord with trend 2. The other studies, such as Yang et al. [135], Hou et al. [33,136], and Du et al. [137], show a trend similar to trend 4; their BTS decreases first to a low value (the

anisotropy angle is around 60°) and then keeps on, unchanged. The BTS from the study of He and Afolagboye [138] shows the variation of trend 3, in which BTS decreases over the entire interval. From the above summary, it can be seen that, although the BTS variation of shale specimens from different sampling sites shows a slight difference, in general, their BTS values do not demonstrate much change from 0° to 30°, and then decrease to a low level around 45°–60°, and finally keep within a stable range around 75°–90°.

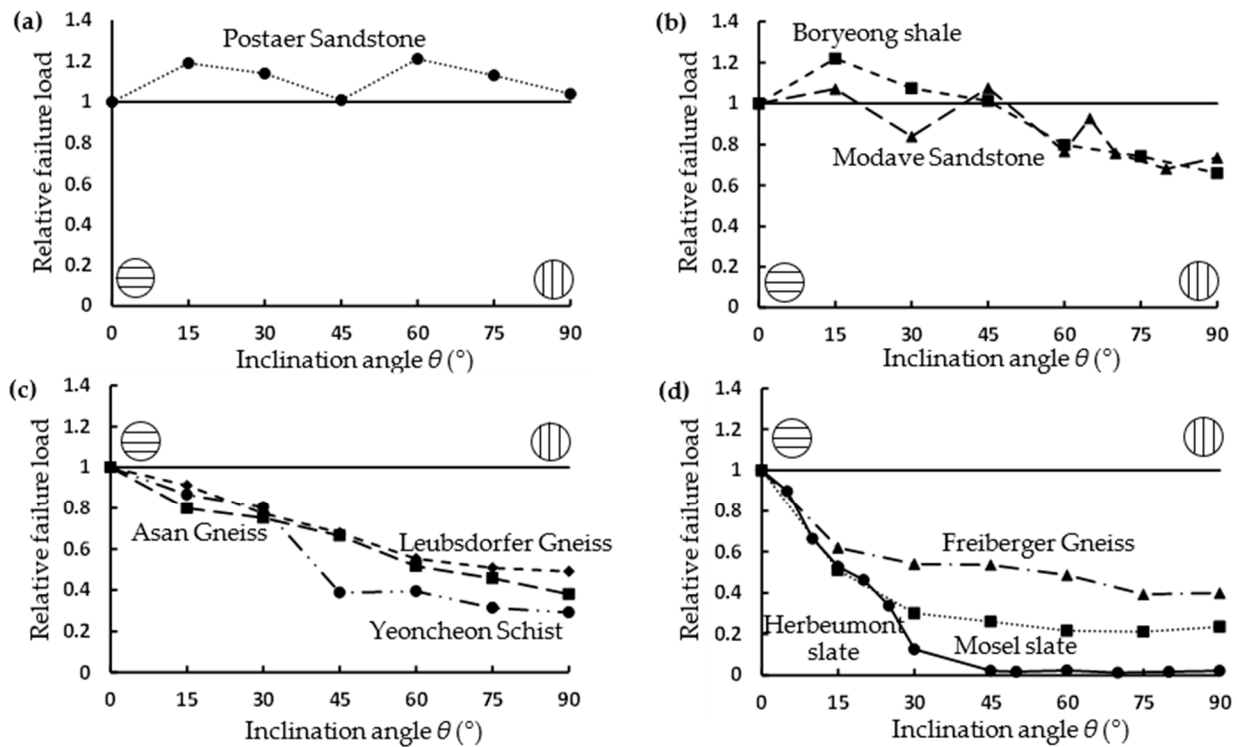


Figure 13. Variation of average failure load, relative to the failure load for loading perpendicular to weak planes: (a) trend 1; (b) trend 2; (c) trend 3; and (d) trend 4 [133].

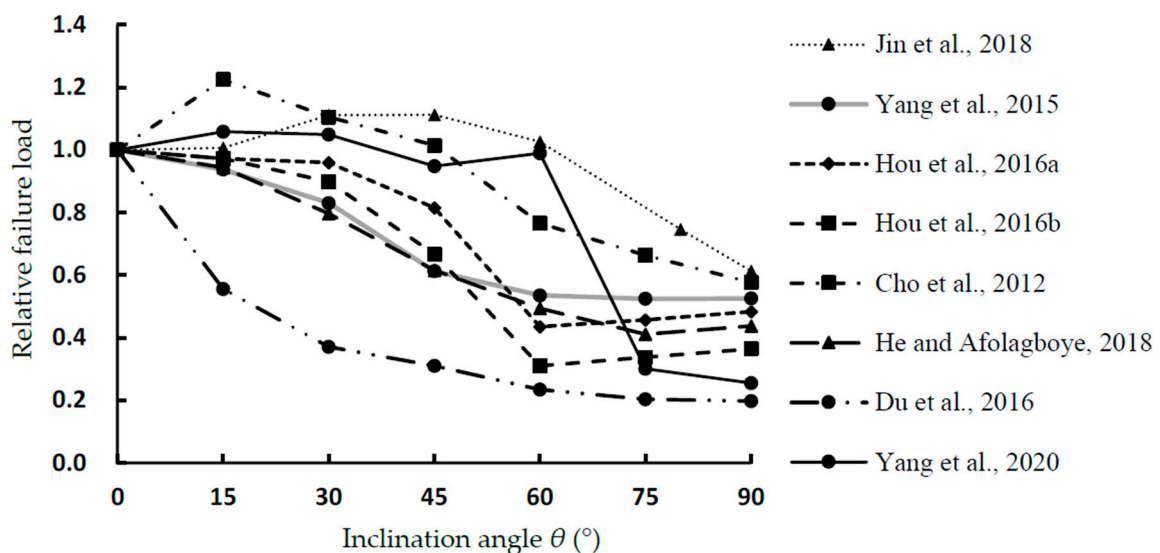


Figure 14. Variation of average failure load, relative to the failure load for loading perpendicular to weak planes, for shale specimens [25,33,81,95,135–138].

To further explain the failure behavior of the shale disc specimen with respect to the bedding plane, the failure pattern in the Brazilian test should be discussed. In the study of Hou et al. [136], shale disc specimens are loaded under Brazilian tests with different

bedding inclinations. They classify the Brazilian split failure process of shale specimens into three stages: compaction, elastic deformation, and destruction stages. Their test results show that the anisotropic characteristics of tensile strength and failure pattern are highly distinct at the peak point of stress. The bedding plane has a strong effect at the bedding inclination of 60° and a weak effect at 0° . They also reported the transformation angles of the failure mechanisms, which are the bedding inclinations of 60° and 45° . At 60° , a tension fracture along the bedding turns to cross the bedding plane, and a cross-bedding plane fracture turns to shear slip at 45° . These findings are similar to those in the studies of Cho et al. [95] on Boryeong shale, Vervoort et al. [133] on Freiburger Gneiss, Du et al. [137] on Shaanxi shale, and Yin and Yang [104] on layered sandstone. Cho et al. [95] investigated the BTS of Boryeong shale under different loading angles. The study's results show that the maximum tensile strength occurs near 15° , and the minimum value occurs when the bedding line is parallel to the axial direction (90°). Additionally, the shale begins to fracture along the bedding when $\theta > 30^\circ$. When $0^\circ \leq \theta \leq 15^\circ$, the crack propagates along the loading direction.

From the above studies and discussion on the anisotropic characteristics of BTS and failure patterns, it can be concluded that, with the bedding closely aligned to the loading direction, the bedding's effect on the BTS turns out to be significant. In other words, there seems to be a critical loading angle; the BTS could not be affected before the critical angle, and decreases rapidly when it exceeds it. In the research of Yin and Yang [104], many disc specimens of layered sandstone were tested and a critical bedding inclination θ of 71.6° was derived by theoretical analysis. In their studies, to better explain the stress state at the center, the normal and shear stress coefficients k_N and k_S are defined. As shown in Figure 15, when $0^\circ < \theta < 71.6^\circ$, the compressive stress and shear stress are applied on the bedding plane, and the disc specimen can evince tension in the rock matrix and shearing at the bedding; and when $71.6^\circ < \theta < 90^\circ$, the bedding plane is under tensile and shear states simultaneously, and when the shear stress is at a high level, the disc specimen can be shear or tensile along the bedding plane. The bedding may be under compression, shearing, or tension states with respect to the variation of bedding inclination. When the bedding inclination is low, the bedding is dominated by compression, does not easy fail. When at a high bedding inclination, the bedding is under shearing and tension simultaneously, and easily experiences shear slip and tensile split.

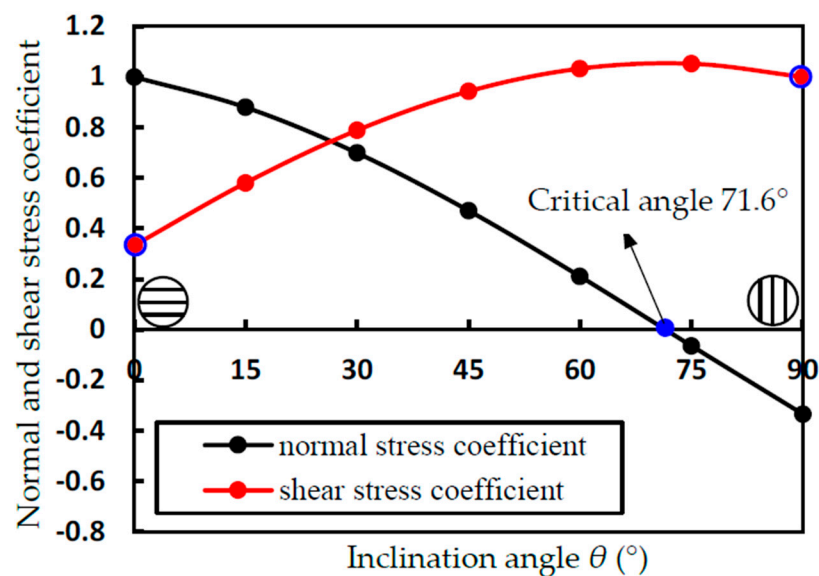


Figure 15. The variation of the stress state at the center with respect to bedding inclination [104].

Figure 16 presents some failure examples for shale disk specimens under the Brazilian test, with different bedding inclinations from different studies shown. From these fractured disk specimens with different loading directions, it can be seen that the fracture pattern of

the anisotropic rock is much different from those of isotropic rock. Although the fractures generally propagate along the loading direction, the bedding directions have distinct effects on the fracture propagation to a certain extent. In some specimens with high bedding inclinations of 60° and 75° , such as the Mancos and Boryeong Shale with 60° (Figure 16a from Simpson et al. [139] and Figure 16b from Cho et al. [95]), Chongqing shale with 75° (Figure 16c from Hou et al. [136] and Figure 16d from Wang et al. [32]), the fractures extend along or divert to the bedding planes. The principal reason for this pattern is that the bedding plane is very closely aligned to the loading direction when under a high bedding inclination, and the shear stress or tensile stress is dominant in the bedding plane and this easily leads to shear or tensile fracture along it. This is in accord with the study and explanation of Yin and Yang [104] in Figure 15.

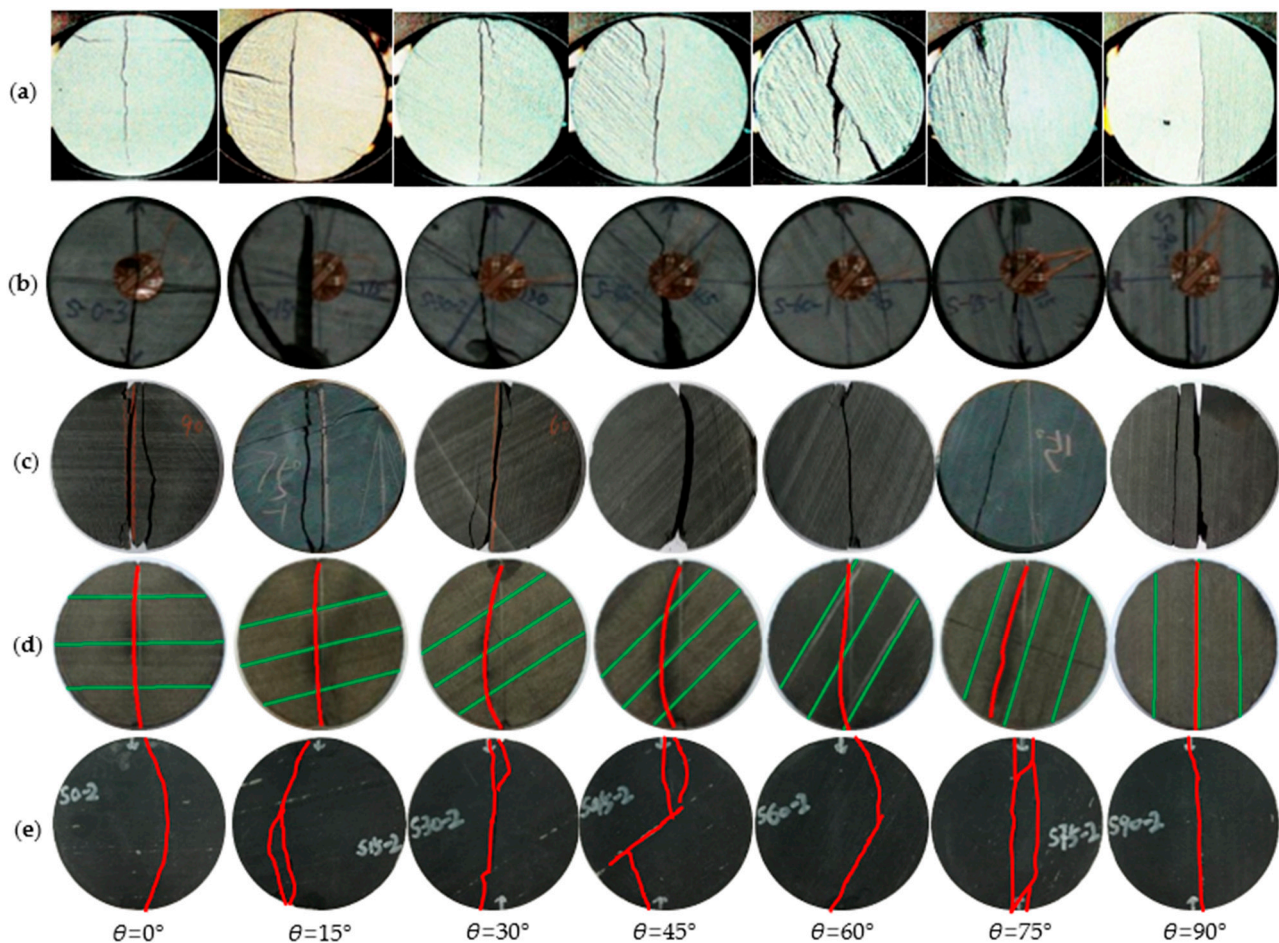


Figure 16. Examples of the failed disk specimen under the Brazilian test: (a) Mancos shale from Simpson et al. [139], (b) Boryeong shale from Cho et al. [95], (c) Longmaxi Formation, Chongqing shale from Hou et al. [136], (d) Longmaxi Formation, Chongqing shale from Wang et al. [32], and (e) Changsha shale from Yang et al. [81].

By conducting a series of Brazilian tests on layered sandstone, Tavallali and Vervoort [131] considered the specimens after failure and classified the observed fractures into three different types (see Figure 17): (1) layer activation (LA), in this pattern, the fractures extend along the bedding planes; (2) central fractures (CF), in this pattern, fractures are roughly located in the central part of the specimen and parallel to the loading direction; (3) non-central fractures, in these cases, the fractures are outside the central part. As shown in Figure 17, the mode of LA mostly occurs at a high loading direction of 60° – 90° , and the mode of CF mostly occurs at a low loading direction of 0° – 30° , while the combination of LA and CF appears at a loading direction of 45° – 75° . The failure modes at $\theta = 0^\circ$ and

90° look similar; these are all central fractures along the loading direction. However, their fracture mechanism is different: the central fracture in specimen $\theta = 0^\circ$ extends across the beddings, which shows the rock matrix fractured by tension; and the central fracture in specimen $\theta = 90^\circ$ extends at the beddings, which shows the bedding fractured by tension and is more in accord with the layer activation. This is also can be explained by Figure 15: the BTS of $\theta = 0^\circ$ is rather similar to the BTS of the rock matrix, and the BTS of $\theta = 90^\circ$ corresponds least to the BTS of the bedding plane [131].

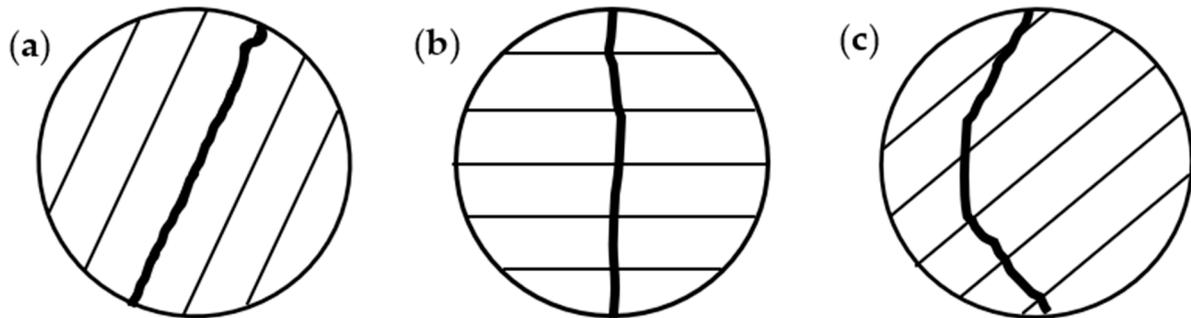


Figure 17. Schematic patterns of different fracture types in the Brazilian test [131]: (a) Layer activation (LA), (b) Central fracture (CF), and (c) Non-central fracture.

3.4. Fracture Toughness Anisotropy of Shale Specimens

The fracture toughness of mode I (K_{Ic}), is an important parameter that controls the hydraulic fracture propagation [140,141]. To determine the K_{Ic} of brittle rock material, many experimental methods and configurations have been designed; some common methods and their configurations are listed in Table 2. As described in Table 2, the configurations of CCCD, SCB, and SENB are specimens with straight-through notches, and the others are specimens with chevron notches. To make sure that fracture behavior can be characterized appropriately by the linear elastic fracture mechanics (LEFM), large specimens are selected, such as deep beam of NBD and CNDB.

Table 2. Summary of some common test methods and configurations for K_{Ic} determination of a rock specimen.

Methods and Specimen Configuration	Graphic Illustration	References
Centrally cracked circular disc (CCCD)		Awaji and Sato [142], Atkinson et al. [143]
Semicircular bend specimens (SCB)		Chong and Kuruppu [144], Lim et al. [145], Dai et al. [146], Funatsu et al. [147], Ren et al. [148]
Single-edged notched beam specimens (SENB)		ASTM [149]
Straight edge cracked round bar bending specimens (SECRBB)		Bush [150]
Single edge-notched deep beam specimens (SENDB)		Luo et al. [37,151]

Table 2. Cont.

Methods and Specimen Configuration	Graphic Illustration	References
Chevron-notched beam specimens (CNB)		Wu [152]
Chevron-notched deep beam specimens (CNDB)		Ren et al. [153]
Cracked chevron-notched Brazilian disc specimens (CCNBD)		Sheity et al. [154], Fowell [155], Dai et al. [156]
Chevron-notched semicircular bend specimens (CNSCB)		Kuruppu [157], Dai et al. [158]
Short-rod specimens (SR)		Barker [159], Ouchterlony [160]
Traditional Brazilian disk and flatted disk specimens without pre-existing flaws		Wang and Xing [161]

To determine the fracture toughness anisotropy of the shale specimens, three main crack orientations can be designed [162], as shown in Figure 18: arrester, divider, and short-transverse. By conducting loading tests on these three kinds of specimens using the different methods listed in Table 2, the fracture toughness tested in different crack orientations shows distinct differences. The fracture toughness of specimens with cracks oriented parallel to the bedding plane (short-transverse, Figure 18c) is smaller than in the other two crack orientations [54,151,153,162,163]. This result is easy to understand, and the reason for it is that the specimens with a pre-existing crack parallel to the bedding planes are easy to initiate, due to the weak tensile strength of the bedding plane [164].

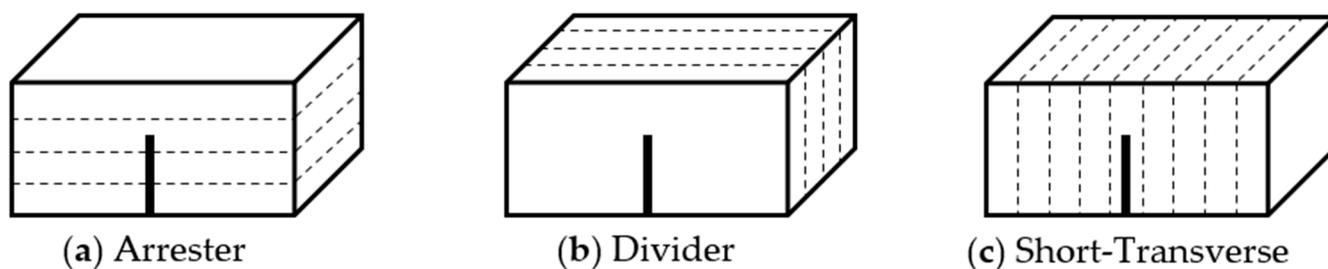


Figure 18. Sketch of the specimens with three main pre-existing crack orientations: (a) Arrester, (b) Divider, and (c) Short-Transverse.

From Figure 18, we can see that in the case of Arrester (Figure 18a), the crack extends through the isotropic plane (bedding plane). In the case of Divider (Figure 18b), the crack also propagates in the rock matrix but does not need to extend through the bedding plane. Thus, comparing the cases of Arrester and Divider, the crack propagation is slightly harder in Arrester, as the crack needs to expend more energy to penetrate through the isotropic plane. This is clearly illustrated in Table 3, which summarizes experimental results from various studies conducted using different testing methods. From Table 3, it

can be found that almost all the fracture toughness values of $K_{Ic, A}$ are greater than $K_{Ic, D}$, while, meanwhile, their ratio is nearly always around 1, which indicates that the crack propagation in Arrester and Divider is dominated by the rock matrix. On the other hand, it can be clearly seen that in the case of Short-Transverse (Figure 18c) the crack initiation and propagation are mainly needed to open the beddings, and this expends less energy than used in the other two cases due to the weak tensile strength of bedding plane. Thus, as displayed in Table 3, the value $K_{Ic, ST}$ is much lower than the $K_{Ic, A}$ and $K_{Ic, D}$.

Table 3. Summary of the shale rock K_{Ic} values obtained from different studies.

Shale Material	References	Bedding Orientation	Method	K_{Ic} (MPa·m ^{1/2})	Fracture Toughness Ratios			
					$K_{Ic, A}/K_{Ic, ST}$	$K_{Ic, D}/K_{Ic, ST}$	$K_{Ic, A}/K_{Ic, D}$	
Longmaxi shale	Luo et al. [37]	Arrester	NDB	1.661	1.952	--	--	
		Short-Transverse		0.851				
	Heng et al. [45]	Arrester	SECRBB	1.146	2.025	1.691	1.198	
		Divider		0.957				
	Wang et al. [165]	Short-Transverse	CCNDB	0.566	1.313	--	--	
		Arrester		0.9226				
	Wang et al. [165]	Short-Transverse	SCB	0.7028	1.267	--	--	
		Arrester		0.8297				
	Dou et al. [166]	Short-Transverse	SENB	0.6549	1.476	--	--	
		Arrester		1.366				
	Ren et al. [153]	Short-Transverse	CNDB	0.927	1.487	1.429	1.041	
		Arrester		1.161				
Chandler et al. [54]	Divider	SR	1.116	3.667 (ST, low)	3.667 (ST, low)	1.000		
			Short-Transverse				0.781	
	Short-Transverse (low)	SR	0.44	1.419 (ST, high)	1.419 (ST, high)	1.000		
			Short-Transverse (high)				0.12	
Mancos shale	Chandler et al. [163]	Divider	Double-torsion specimen	0.31	--	1.297	--	
		Short-Transverse		0.48				
	Li et al. [167]	Arrester	SENB	0.37	0.995	1.309	0.760	
		Divider		0.912				
	Lee et al. [53]	Short-Transverse	SCB (25.4 mm in diameter)	1.200	--	--	2.0099	
		Arrester		0.917				
Nash Point shale	Inskip et al. [168]	Divider	SCB (38.1 mm in diameter)	0.944	--	--	1.207	
		Arrester		0.470				
	Short-Transverse	SCB	0.479	3.083	2.958	1.042		
			Arrester				0.74	
Anvil Points shale (80 mL/kg kerogen content)	Schmidt [162]	Divider	SENB	0.71	1.303	1.435	0.908	
		Short-Transverse		0.24				
	Anvil Points shale (160 mL/kg kerogen content)	Schmidt [162]	Arrester	SENB	0.73	1.632	1.822	0.896
			Short-Transverse		0.30			
Anvil Points shale (160 mL/kg kerogen content)	Schmidt [162]	Arrester	SENB	0.977	1.632	1.822	0.896	
		Short-Transverse		1.076				

As for other anisotropic directions of crack propagation, Lei et al. [169] have conducted investigations regarding the fracture behavior of shale samples with different bedding strengths. Their beam specimens are processed with different bedding inclinations according to the straight-through notch and tested under three-point bending loading. The micro-crack propagation process was observed by the SEM equipment with a loading system. The results revealed that the outcrop shale of the Longmaxi Formation from Pengshui County, in the southeast of Chongqing, China, shows strong anisotropy and that this has a great effect on hydraulic fracture propagation. In Figure 19a, it can be observed that the micro-cracks initiate at the notch tip, and then propagate along the loading direction. Figure 19b shows the simulated failure patterns of three-point bending specimens under different bedding properties. The tensile strength of the smooth joint decreases from mode I to mode IV. The results revealed that the fracture characteristic of shale is affected by bedding inclination and bedding strength. It is also can be determined that the cracks exhibit strong tortuosity under a low tensile strength of the bedding plane.

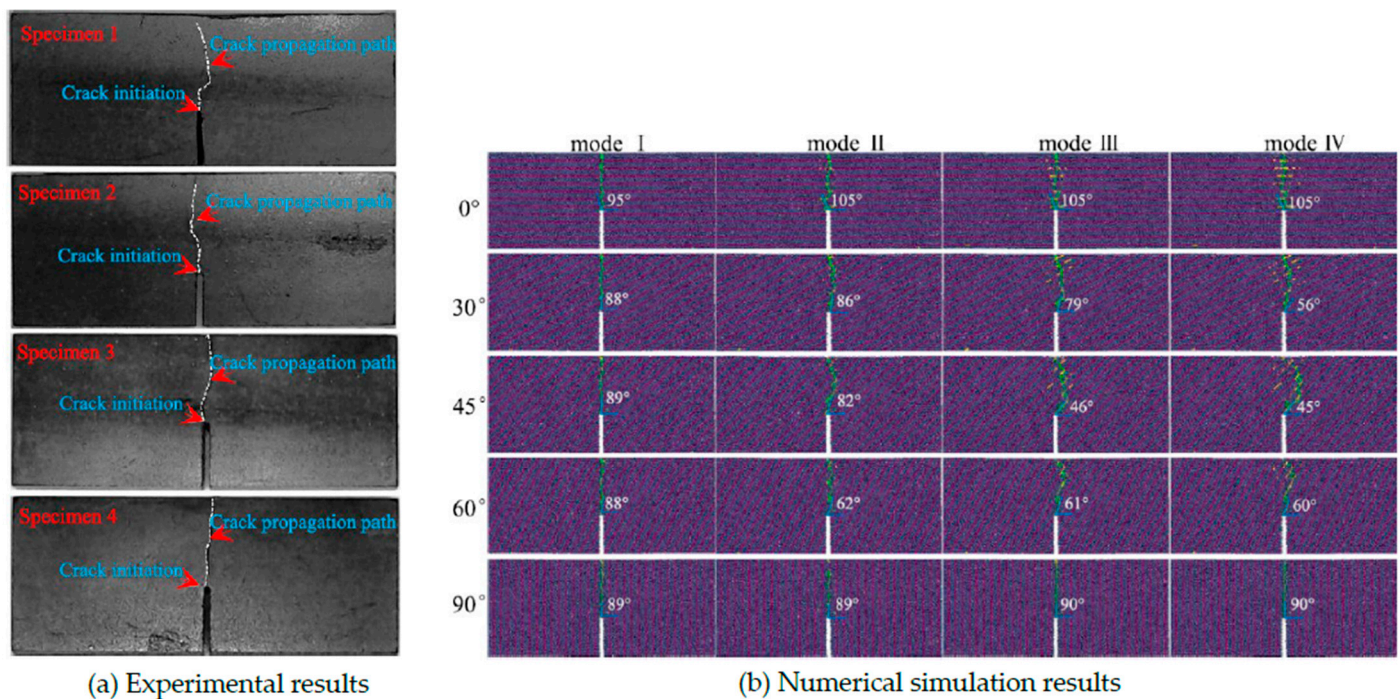


Figure 19. Failure patterns under different bedding properties [169].

On the other hand, as shown in Figure 20a, the study results of Lei et al. [169] reveal that, when under the same bedding strength, the fracture toughness decreases with the increases of bedding inclination, with a maximum at 0° and a minimum at 90° . Particularly, the fracture toughness decreases gently between 0° and 45° , and then decreases rapidly after 45° . It indicates that when the bedding inclination approaches the loading direction, the bedding's effect on fracture toughness turns to be more obvious. It can be clearly seen from Figure 19b that the crack propagation eventually occurs at the bedding planes more obviously when the bedding inclination increases after 45° . In particular, as displayed in Figure 19b, mode IV has the lowest bedding strength, resulting in the most obvious crack deflection towards the bedding plane. Luo et al. [37] and Shi et al. [170] have investigated fracture toughness anisotropy under different bedding inclinations. The shale specimens used by Luo et al. [37] and Shi et al. [170] are all sampled from the Longmaxi Formation. The former study processed NDB shale specimens, with a length-to-width ratio (L/W) of 2.0 and an edge crack with inclined angle $\alpha = 0^\circ$ and bedding inclination $\theta = 0^\circ, 30^\circ, 60^\circ$, and 90° . The latter study employed the CCNBD specimens with chevron notches with angles of $0^\circ, 30^\circ, 45^\circ, 60^\circ$, and 90° . Figure 20b depicts the K_{Ic} variations concerning the shale bedding inclination from the above two studies. The results show that the bedding inclination has a distinct effect on the fracture toughness, and the tested values all decrease with an increase of bedding inclination.

In the above studies, the test specimens with bedding inclinations of 0° and 90° are configured in accord with the cases of Arrestor (shown in Figure 18a) and Short-Transverse (shown in Figure 18c), respectively. It can be determined from Figure 20 that the maximum value is at 0° and the minimum at 90° , which is in accord with the findings from Table 3. The crack's approach angle relative to the bedding plane and bedding strength are the key influence factors in hydraulic fracture propagation. The high approach angle and low bedding strength contribute to the fracture propagation along bedding planes. The Short-Transverse specimen has the lowest fracture toughness, due to the weaker bedding plane, and has a looser grain arrangement and is less resistant to crack propagation [171]. The microcracks could extend and coalesce, resulting in the failure of grain clusters [172].

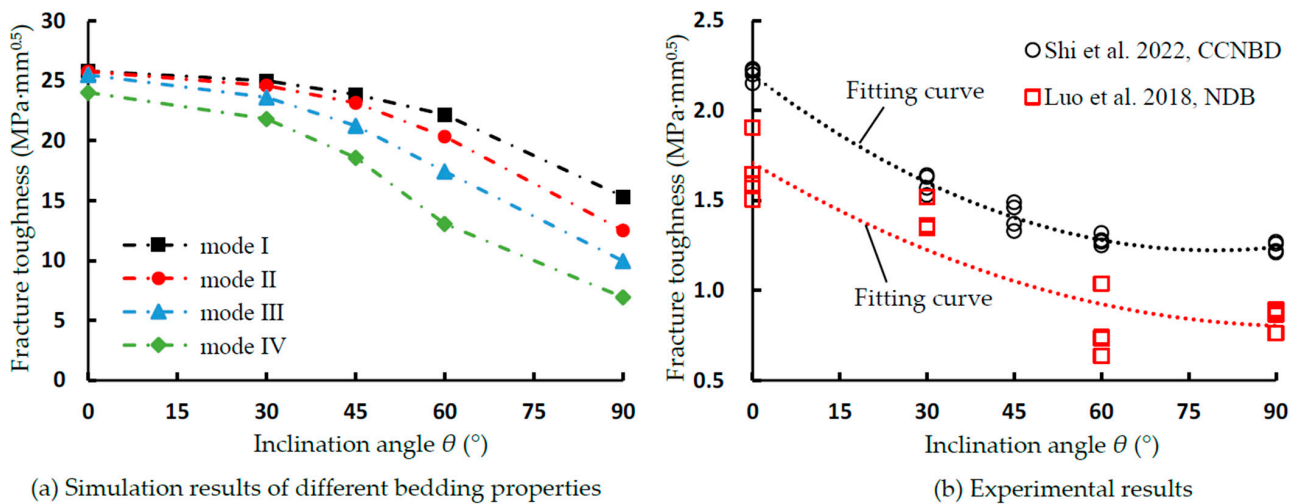


Figure 20. Variation of K_{IC} with respect to the bedding inclination of the shale specimen [37,170].

4. The Relationship of Shale Mechanical Properties to Hydraulic Fracturing Evaluation

4.1. Quantitative Evaluation of Shale Brittleness Based on Mechanical Properties

Brittleness is commonly applied to characterize the failure behavior of the rock material [173]. For hydraulic fracturing, the high brittleness of shale may contribute to the deeper and more complex fracture propagation. Therefore, the evaluation of brittleness is important in engineering. Based on various previous studies, brittleness can be defined as the lack of ductility [174,175], as a failure at or only slightly exceeding the yield stress [176], as the cohesion destruction [177], as a failure with small or no plastic deformation [178], and as a self-sustaining failure process [179].

As for hydraulic fracturing in shale, the brittleness index (BI) is usually employed to quantify the brittleness degree of rock, which is useful for evaluating the ability of fracture propagation (fracability) and fracture network generation. To accurately measure the brittleness of shale rock, many factors should be considered. To date, many BIs have been proposed to quantify its extent [73,179–187]. Table 4 lists some common BIs, mainly based on mineral composition, and strength parameters.

Among the test methods in Table 4, mineral composition is easy to obtain and can be precisely determined by conducting laboratory analyses such as XRD testing. Methods based on strength parameters, stress–strain characteristics, and energy balance analysis can be determined by stress–strain curves. As the stress–strain curves can be obtained easily by conducting the triaxial compression test, this measurement is commonly used to determine strength parameters. The brittleness is a mechanical response to a specific stress state. For a material, the composition is constant, but the brittleness can vary if different stress states are applied. Therefore, the specific stress state must be considered when its brittleness is evaluated. Thus, BI definitions based on stress conditions, such as strength parameters, stress–strain characteristics, and energy balance analysis, are more significant [2].

As for the brittleness indices $BI_5 \sim BI_9$, which are based on strength parameters, parameters such as UCS and BTS are easily obtained by a laboratory test. All of these BIs display a positive relationship [179] with confining pressure. On the other hand, rocks that show different stress–strain curve shapes may be of the same BI values ($BI_{11} \sim BI_{13}$). Furthermore, the combination of strength and strain performances (BI_{10} and BI_{13}) is more precise in predicting rock brittleness [173]. Additionally, some BIs based on stress–strain ($BI_{11} \sim BI_{13}$) and energy balance (BI_{17}) only consider the effect of the pre-peak state and ignore the stress drop rate; however, some rock materials show a distinct ductility when high confining pressures are applied [185,195].

Table 4. Summary of some universal BI definitions.

Test Method	Formulae	References	Remarks
Mineral composition	$BI_1 = W_Q / W_{Q+C+Cl}$	Jarvie et al. [47]	W_x = weight fraction of component x ; Q = quartz; C = carbonate; Cl = clay; Dol = dolomite; TOC = total organic carbon; Lm = limestone; QFM = quartz+feldspar+mica
	$BI_2 = (W_Q + W_c) / W_{total}$	Rickman et al. [73]	
	$BI_3 = (W_Q + W_{Dol}) / W_{Q+Dol+Lm+Cl+TOC}$	Wang and Gale [188]	
	$BI_4 = W_{QFM+C} / W_{total}$	Jin et al. [189]	
Strength parameters	$BI_5 = \sigma_c / \sigma_t$ $BI_6 = (\sigma_c - \sigma_t) / (\sigma_c + \sigma_t)$ $BI_7 = \sin(\varphi)$ $BI_8 = \sigma_c \sigma_t / 2$	Hucka and Das [180]	σ_c = uniaxial compressive strength; σ_t = Brazilian tensile strength; φ = internal friction angle; ρ = density
	$BI_9 = 0.198\sigma_c - 2.174\sigma_c + 0.913\rho - 3.807$	Yagiz [184]	
	$BI_{10} = (\sigma_f - \sigma_r) / \sigma_f$	Bishop [190]	
	$BI_{11} = \varepsilon_e / \varepsilon_f$	Hucka and Das [180]	
Stress–strain characteristics	$BI_{12} = \varepsilon_p \times 100\%$	Andreev [191]	ε_p = sustained plastic strain at failure; ε_e = total elastic strain; ε_f = total strain at failure; ε_r = residual strain; σ_f = stress at failure; σ_r = residual strength E = elastic modulus; M = post-peak modulus
	$BI_{13} = (\varepsilon_f - \varepsilon_r) / \varepsilon_f$	Andreev [191]	
	$BI_{14} = E / v$	Luan et al. [192]	
	$BI_{15} = E / M$	Tarasov and Potvin [179]	
	$BI_{16} = (M - E) / M$		
Energy balance analysis	$BI_{17} = U_{et} / (U_{et} + U_p)$	Hucka and Das [180]	U_{et} = total elastic energy; U_p = plastic energy; U_r = rupture energy; U_{ec} = consumed elastic energy; U_a = additional energy;
	$BI_{18} = U_r / U_{ec}$ $BI_{19} = U_a / U_{ec}$	Tarasov and Potvin [179]	
	$BI_{20} = U_{et} / (U_r + U_p)$ $BI_{21} = (U_{et} + U_p) / (U_r + U_p)$ $BI_{22} = U_{et} / U_r$	Munoz et al. [193]	
	$BI_{23} = (U_r + U_p) / (U_{ec} + U_p)$ $BI_{24} = U_a / (U_{ec} + U_p)$	Ai et al. [194]	

The drilling of horizontal wells for hydraulic fracturing in shale usually needs to cross bedding planes in different orientations; thus, the shale anisotropy should not be ignored in a brittleness evaluation [50]. According to the various studies on anisotropic mechanical properties of shale specimens from Sections 3.2 and 3.3, the UCS shows a “U” type variation and BTS shows a negative relationship with bedding inclination. Thus, as illustrated in Figure 21, from the equations of the BI_5 and BI_6 in Table 4, which are calculated by UCS and BTS, it can be concluded that the variation of the two BIs concerning bedding inclination will display a similar “U” type. Before the inflection point, the UCS and BTS decrease, and the UCS decreases faster than the BTS; therefore, the BI_5 and BI_6 decrease gently. When the bedding inclination increases to a high level, such as 90° , the BTS decreases to a very low level and UCS is at a high level; thus, the BI_5 and BI_6 increase to high magnitudes rapidly. It should be noted that the BI_5 and BI_6 variations before the inflection point closely depend on the margins of UCS and BTS reductions; as shown in Figures 8 and 14, the UCS and BTS reduction from various shale specimens are different. Therefore, in Figure 21 the BI_5 and BI_6 variation before the inflection point may show a decrease or a gentle increase, or, alternatively, it can be stable.

In the study on shale brittleness evaluation from Yang et al. [2], the researchers obtained data from the triaxial compression test. They proposed two new brittleness indices, BI_1^* and BI_2^* , to evaluate the shale brittleness variation with respect to bedding inclinations. By comparing the two new brittleness indices with the BI from Kivi et al. [49], which is referred to herein as BI_{25} , the BI variation concerning bedding inclinations is depicted in Figure 22. The new brittleness indices BI_1^* and BI_2^* from Yang et al. [2] and BI_{25} from Kivi et al. [49] are expressed as follows:

$$BI_1^* = \frac{\sigma_f - \sigma_r}{\sigma_f} \lg|M| \quad (6)$$

$$BI_2^* = U_{ei} / (U_{et} + U_p) \tag{7}$$

$$BI_{25} = 0.5(U_{ec}/U_r + U_{ec}/(U_{et} + U_p)) \tag{8}$$

where σ_f is the strength and σ_r is the residual strength, respectively, and M is the modulus after the peak. U_{ei} is the ideal elastic energy, as defined in Yang’s study. [2]. The other parameters are noted in Table 4.

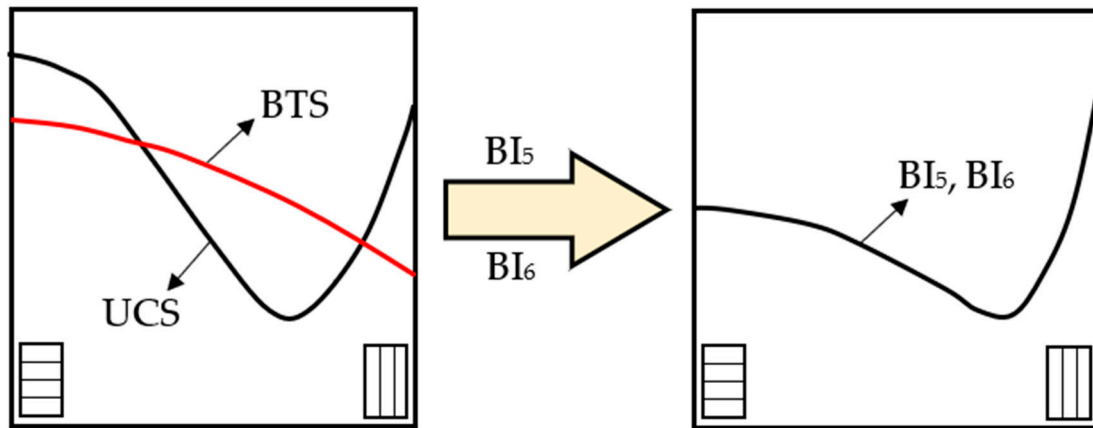


Figure 21. Shale brittleness variation with respect to bedding inclinations, using BI_5 and BI_6 .

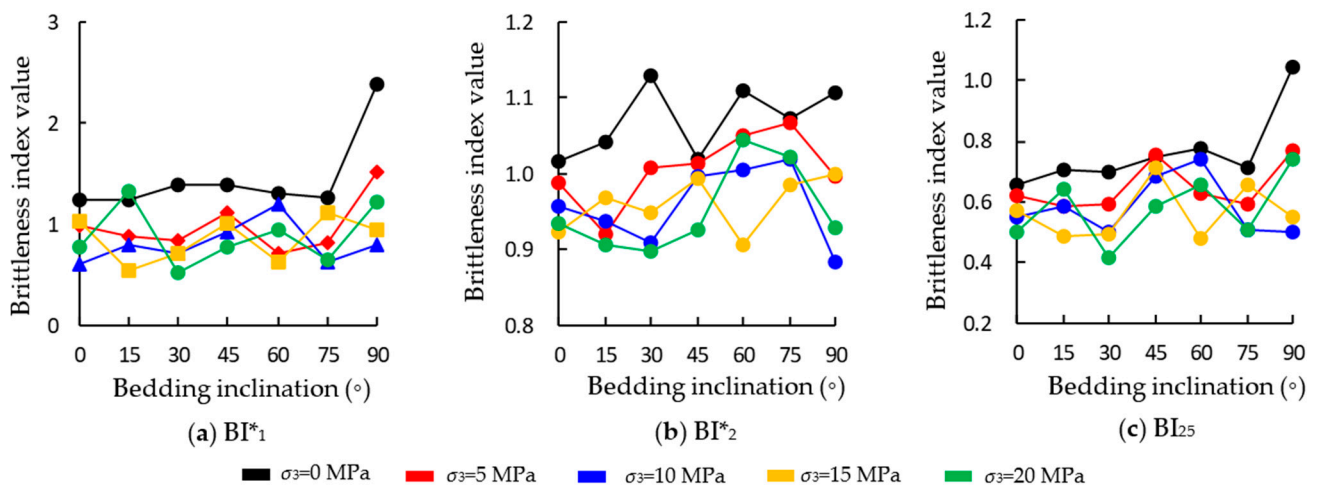


Figure 22. Shale brittleness variation with respect to bedding inclinations, using different BIs [2].

From Figure 22a,c, we can see that the BI_1^* and BI_{25} display very similar variations, roughly increasing with respect to the bedding inclination; in particular, they increase rapidly when the bedding inclination is at 90° . This indicates that the shale specimen shows higher brittleness when the bedding inclination is at a high level. This experimental finding is in accordance with the conclusion stated in Figure 21. In the study of Qian et al. [50], a novel BI is proposed for analyzing the anisotropic characteristics of brittleness [196,197]. Their theoretical research suggests that Young’s modulus in the vertical is lower than that in the horizontal, and Poisson’s ratio in the vertical can be either higher or lower than that in the horizontal. Thus, the BIs, which are determined by parameters of Young’s modulus and Poisson’s ratio, can vary significantly when drilling in shale formations with strong anisotropy.

The brittleness, under uniaxial compressive conditions, which results in tensile failure is higher than the brittleness when confining pressure is applied. Therefore, it can be concluded that the shale specimens that failed by tension show higher brittleness than those that failed by shearing. The reason may be attributed to the shearing slip along

the fracture plane having led to a more plastic deformation. Specimens with fractures extending along the bedding show higher brittleness than those samples with fractures that extend across the bedding. [2]. Therefore, according to the conclusions from Figure 12 and Table 1, the order of brittleness can be as follows: T-A > T-T > S-A > S-T.

4.2. The Anisotropic Effect of Bedding Plane on Hydraulic Fracture Initiation and Propagation of Shale

The weak bedding has a key effect on hydraulic fracturing characteristics [61]. Many researchers have attempted to reveal the relationship between the breakdown pressure and the bedding inclination. A general conclusion has been reported that the breakdown pressure is considered to be decreased with increases of bedding inclination [40,198]. By comparing different experiments results, it is found that the breakdown pressure and BTS show similar variations, in which the maximum values and minimum values occur at the bedding inclinations of 0° and 90° , respectively [40]. However, the breakdown pressure also can be increased first and then decreased relative to the bedding inclination [61]. Figure 23 depicts the relationship of breakdown pressure and bedding inclination. As can be seen in Figure 23, the breakdown pressure first increases and then decreases, as the bedding inclination increases. The maximum and minimum breakdown pressures occur at 45° and 90° , respectively. This variation agrees well with the tendency determined in the research of Chong et al. [199], which synchronously considered the effect of confining pressure and under a condition of $\sigma_v = 20$ MPa, $\sigma_c = 10$ MPa, and $Q_{inj} = 6$ mL/min. In the research of Lin et al. [40] and Zhang et al. [198], the breakdown pressure under triaxial hydraulic fracturing ($\sigma_v = 25$ MPa, $\sigma_c = 20$ MPa, $Q_{inj} = 12$ mL/min) shows a decreasing tendency as the bedding inclination increases. The above two different conclusions reveal that the anisotropy of shale breakdown strength depends on the stress conditions, injection rates, and fluid viscosity [198,200]. However, the breakdown pressure seems to fluctuate within a bedding inclination range from 30° to 60° , and the breakdown pressure, mostly at the bedding inclination of 90° , is minimum. The reason for this variation may be attributed to the effects of tensile strength and the critical stress intensity factor (critical SIF). A smaller bedding inclination contributes to more stress components on the bedding planes, enhancing bedding compression, and thus, higher breakdown pressure is needed to initiate a fracture. Additionally, according to some relative theoretical analysis [201,202], it has been revealed that when $\theta < 45^\circ$, the critical SIF increases as the bedding inclination increases, and when $\theta > 45^\circ$, the critical SIF turns to become smaller as the bedding inclination increases. Higher fluid pressure is needed for the fracture propagation when under higher critical SIF, and then breakdown pressure turns to be at its maximum value at $\theta = 45^\circ$.

There are significant interactions between a hydraulic fracture (HF) and joints, bedding planes (BP), and faults [38]. The development of BP is one of the key factors affecting hydraulic fracturing in shale formation [39]. The angle of the HF as it approaches the BP is generally considered to be an important parameter in determining the interaction between them [203–206]. At a low angle ($<30^\circ$), the HF propagates along the BP, and crosses the BP at a high angle ($>60^\circ$), while at moderate angles ($30^\circ \sim 60^\circ$) the fracture arrests [38,39]. These weak BP would be activated during fracturing if the friction coefficient or cohesion is at a low level, which contributes to creating a complex fracture network [203,205–209]. Wang et al. [210] conducted experiments on shale specimens to investigate the fracturing mechanism and the effect of BP. The shale was marine black carbonaceous with obvious bedding structures, which lead to strong anisotropy. They summarized the fracturing failure patterns after hydraulic fracturing. As shown in Figure 24, the BP induce the HF propagating orientation to change. The HF is of a complex pattern controlled by bedding inclination and stress condition. From the test result, the failure patterns can be summarized as follows: (a) central planar fracture, which mostly occurs when $\theta = 0^\circ$ and 90° ; (b) deflected fracture, which mostly occurs when $\theta \leq 45^\circ$; and (c) layer-activated fracture, which mostly occurs when $\theta > 45^\circ$. It should be noted that the central planar

fracture in the specimen of $\theta = 90^\circ$ is also a layer-activated fracture, which is induced by the vertical bedding planes.

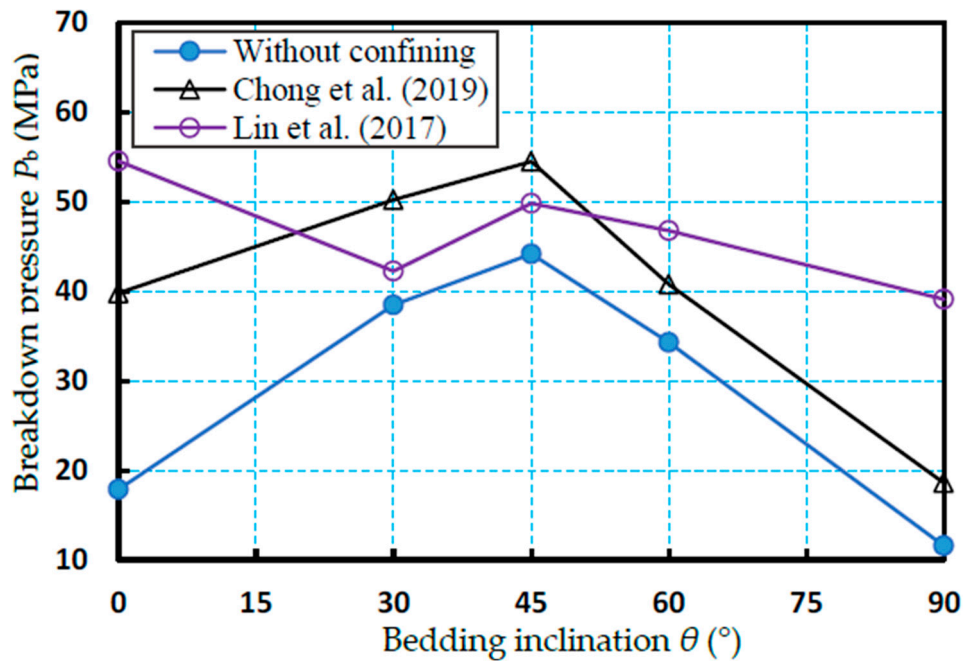


Figure 23. Breakdown pressure variation of shale under different bedding inclinations [40,61].

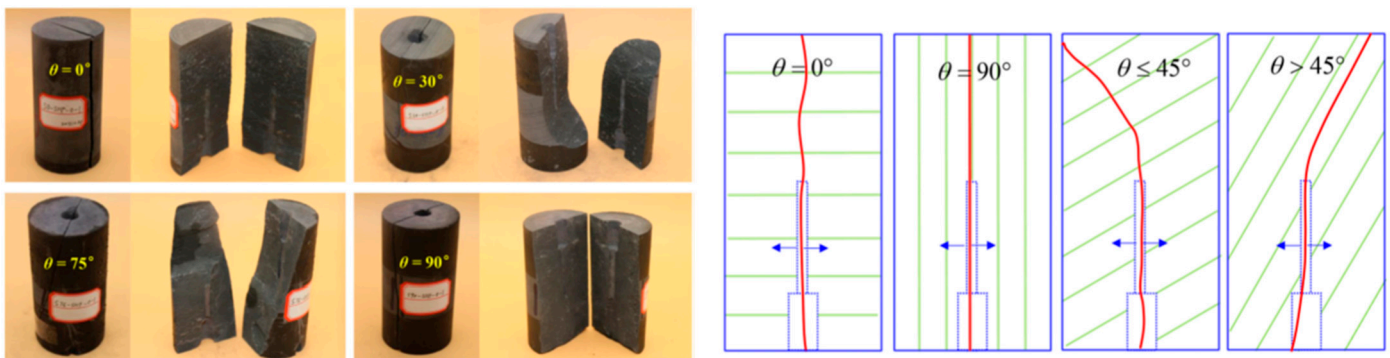


Figure 24. Anisotropic failure patterns of Longmaxi shale in hydraulic fracturing [210].

In general, two propagation modes can be classified when an HF encounters BP, namely crossing and opening. For further classification, as shown in Figure 25, an HF encountering BP can cause four cases: penetration, diversion, offset, and termination [206,211,212]. When under a true triaxial stress condition, the offset mode is observed during the intersection with BP [213]. Penetration (Figure 25a) refers to an HF that crosses the BP but does not change its propagation path. Diversion (Figure 25b) refers to a vertical HF that is deflected into the BP and is divided into two branches. Offset (Figure 25c) refers to an HF re-initiating and leaving a step-over at the BP. To explain these propagation modes, one possible reason is that the shear stress of the interface easily results in HFs crossing the barrier or extending along the BP [203]. Additionally, the strength of the BP may not be the same at different distances, leading to differences in the degree to which the bedding opens [214], and in that case some HFs may cross the BP and some terminate at the BP. The HF propagation is slightly affected by the BP and the natural fracture (NF) when under large vertical and horizontal stress anisotropy conditions [212].

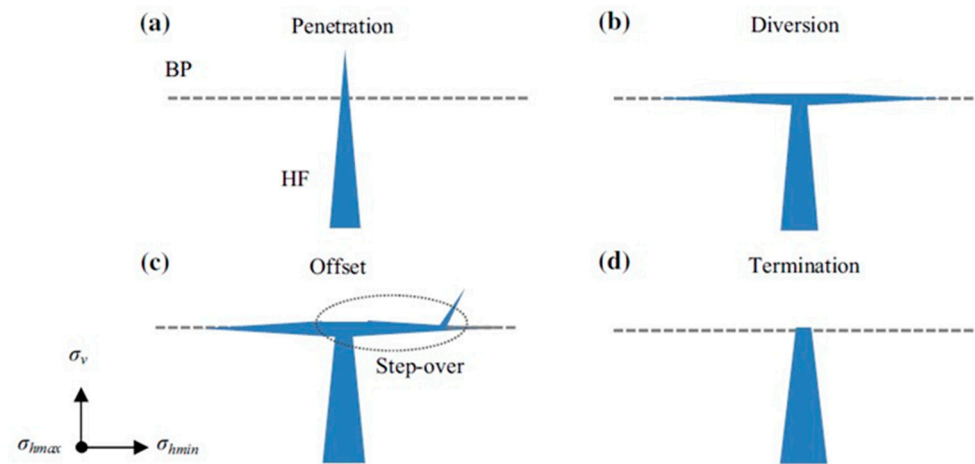


Figure 25. Four basic types of hydraulic fracture intersections with bedding (adapted from Thiercelin et al. [211] and Zou et al. [212]).

For the HF interacting with multi-BP in laminated shale formation, complex fracture networks are of great practical value. The activation of BP is the optimum condition for forming a complex fracture network in the vertical plane [214]. A possible fracture mode is summarized and shown in Figure 26. The depicted four fracture modes are very similar to the fracture types generalized in the study of Yin et al. [215], in which the complex fracture network is formed by primary cross-bedding fractures and secondary interbedding fractures. From the laboratory test results (depicted in Figure 27), it can be determined that interbedding fractures and cross-bedding fractures are generated.

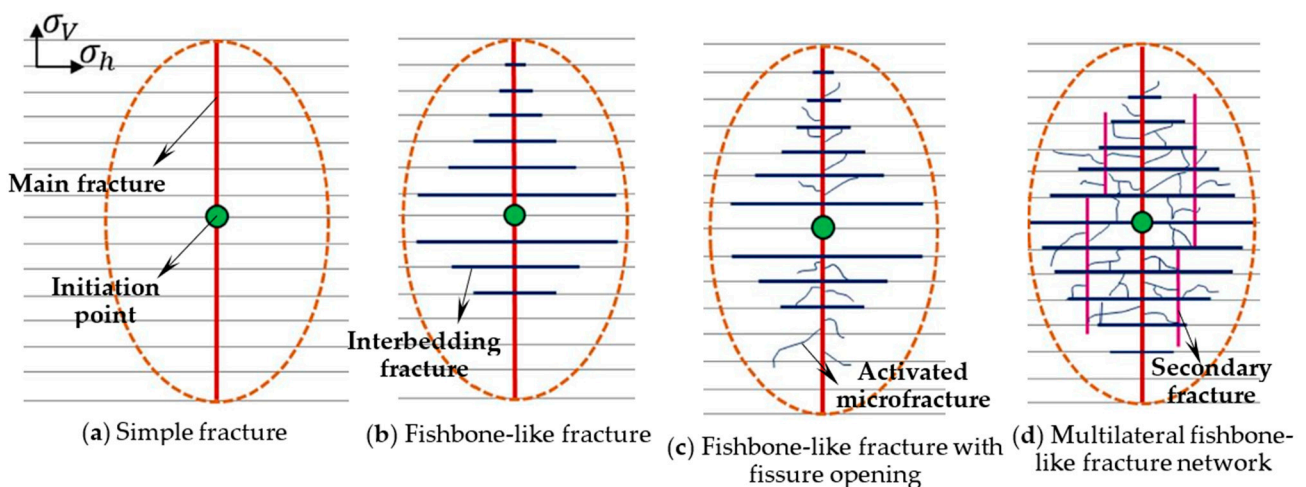


Figure 26. Some basic modes of fracture propagation in a vertical plane, as determined by experiments [214].

The basic HF patterns could be summarized as follows [214] (Figure 28): (1) Mode I (Figure 28a), an HF initiates and propagates perpendicular to the BP; (2) Mode II (Figure 28b), an HF initiates and propagates parallel to the BP; (3) Mode III (Figure 28c), an HF initiates and propagates normal to the BP and a complex fracture network is induced by the weak BP; (4) Mode IV (Figure 28d), an HF initiates and propagates parallel to the BP, and diverts into another propagation path when it meets a cemented fracture; and (5) Mode V (Figure 28e), an HF initiates and propagates from a few NFs, and is diverted into another propagation path by BP. To form the above patterns, the BP strength is the key: In the cases of Mode I and Mode III, the cement strength of the BP should be high, but in Mode III some weak points should be presented. In the cases of Mode II and Mode IV, the cement strength of the BP should be low, but some strong cement BP should be presented in Mode IV. In the case of Mode V, weak NFs occur near the initiation point and the cement

of the BP is low. The above summaries are also consistent with the simulation results of Yin et al. [215], which reveal the important effect of the mechanical properties of BP on the propagation of HF. Additionally, the BP failure was closely related to its cohesion and friction coefficient. If the BP had a low friction coefficient or low cohesion, shear failure would obviously increase. If the cementing strength of the BP at different distances is not the same, the degree of the bedding opening would differ [206,216].

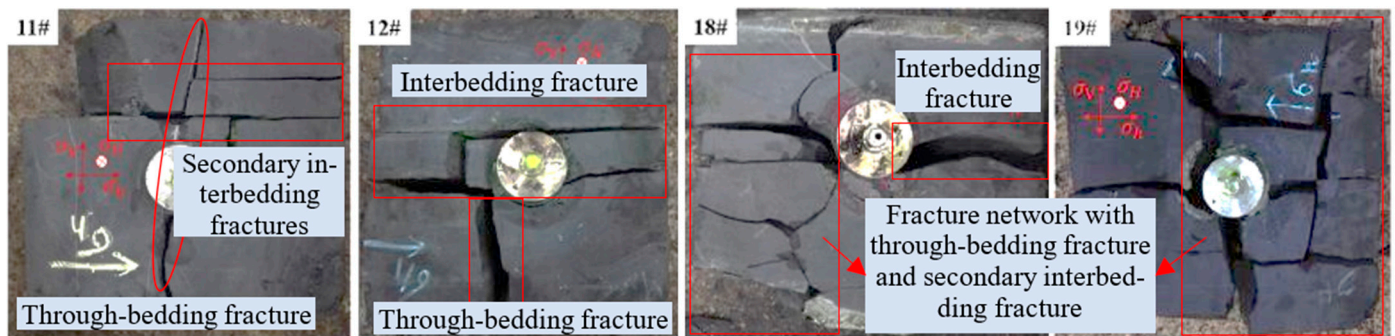


Figure 27. Hydraulic fracture network formed by interbedding fractures and cross-bedding fractures in experiments [214].

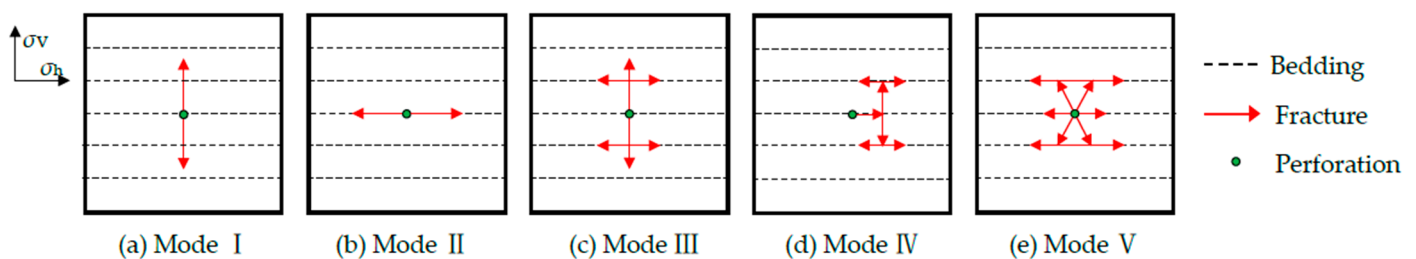


Figure 28. Basic model of hydraulic fracture propagation [214].

5. Conclusions

The efficient implementation of hydraulic fracturing is the key issue in the exploration of shale gas. The existence of bedding structure results in distinct anisotropy of the shale rock formation. The anisotropy has an important influence on wellbore stability and hydraulic fracturing implements. This paper first briefly reviews the previous research works on the lithological characteristics and anisotropic mechanical behavior of shale specimens, and then a brief discussion on the relationship of shale anisotropic mechanical properties to hydraulic fracturing evaluation is conducted. The concerns of anisotropic mechanical behaviors under laboratory tests are addressed; in particular, the evaluation of shale brittleness based on mechanical characteristics is discussed in detail. Further concerns, such as the bedding's effect on the hydraulic fracturing failure strength, crack propagation, and fracture pattern are also drawn. Some main conclusions are drawn, as follows:

(1) The rock mineralogy is critical for the intrinsic formation of anisotropy in shale rock. The proportions of quartz–carbonates–clays could result in very different rock mechanical properties. Clay-rich shale mostly contains highly developed weak planes. Shale samples containing high levels of quartz and low levels of clay have a relatively high Young's modulus and low Poisson's ratio, contributing to a high brittleness and helping hydraulic fracture propagation.

(2) The anisotropy of the wave velocity is thought to result in some geophysical interpretative problems for shale. The effects of mineral grain inclination and micro-cracks are the main factors attributed to an anisotropy. The wave velocities parallel to the bedding are higher than those normal to the bedding, as the ultrasonic wave energy is attenuated by the bedding's scattering. The attenuation anisotropy is affected by the stress, the bedding inclination, and the aspect ratios of micro-cracks.

(3) The mechanical properties of shale specimens under compression show distinct anisotropy. Most determinations of the compression strengths of shale specimens display a “U” type or a similar “shoulder” type variation trend with increasing bedding angle. Particularly, the maximum peak strength is observed at a θ of 0° or 90° , and the minimum values are observed at $45^\circ < \theta < 75^\circ$. The elastic modulus shows an increasing variation with the bedding inclination increases overall; this is in accord with the variation of ultrasonic velocities. The confining stress reduces the anisotropy of rock material, as the confining pressure is hydrostatic pressure, and when it is applied to the specimen, the beddings are compacted, resulting in the reduction of the primary defects effect. The fracture propagation during the failure process is generally affected by the bedding inclination and confining pressure. For bedding inclination of $0^\circ < \theta < 30^\circ$, tensile fracture along the loading direction occurs under low confining pressure, and shear fracture across the bedding plane occurs under high confining pressure; for a bedding inclination of $30^\circ < \theta < 75^\circ$, the fracture generally occurs by the sliding of the bedding, although shear fracture in the matrix can occur, and may cross the bedding; for $75^\circ < \theta < 90^\circ$, the failure occurs by bedding splitting when under low confining stress, and by bedding shearing under high confining stress.

(4) The tensile strength has a distinct effect on fracture initiation and propagation. The BTS variation in shale specimens from different sampling sites shows a slight difference; in general, their BTS values do not have much change from bedding inclination of 0° to 30° , and then decrease to a low level around 45° – 60° , and finally keep within a stable range of around 75° – 90° . The center of the disc specimen is in a compressive state when under low bedding inclination and experiencing shearing and tension when under a high bedding inclination. The layer activation occurs under a high bedding inclination, and the central fracture occurs under a low bedding inclination.

(5) The value $K_{Ic, ST}$ is much lower than the $K_{Ic, A}$ and $K_{Ic, D}$; additionally, $K_{Ic, A}$ is slightly greater than $K_{Ic, D}$. The bedding inclination has a distinct effect on the fracture toughness, the values for which all decrease as the bedding inclination increases. The high approach angle and low bedding strength contribute to the fracture propagation along the bedding planes.

(6) In shale hydraulic fracturing, the brittleness index (BI) is usually employed to quantify the brittleness of the shale rock formation, for the purpose of evaluating the possibilities of fracture propagation (fracability) and fracture network generation. The BI definitions considering mechanical response are more significant. The horizontal well for hydraulic fracturing usually crosses the bedding plane in different orientations; thus, shale anisotropy should not be ignored in brittleness evaluation. The BIs, which are determined by parameters of Young’s modulus and Poisson’s ratio, can vary significantly when drilling in shale formations with strong anisotropy.

(7) The bedding planes (BP) have an important effect on the fracturing characteristics. The breakdown pressure shows a similar variation with the BTS of shale specimens, in which the maximum and minimum values occur at the bedding inclinations of 0° and 90° , respectively. A smaller bedding inclination contributes to more stress components on the bedding planes, enhancing compression on the beddings and resulting in higher breakdown pressure. The bedding shear stress has an important effect on whether the HFs cross the rock formation or extend along the BP, as well as the fact that the strength of the BP may not be the same at different distances, leading to differences in the bedding opening, in which case some HFs may cross the BP and some terminate at the BP. Moreover, the activation of the BP is the optimum condition for forming fracture networks, as opposed to a simple fracture.

Author Contributions: Conceptualization, P.-F.Y. and S.-Q.Y.; methodology, P.-F.Y., S.-Q.Y., and P.G.R.; investigation, P.-F.Y. and S.-Q.Y.; writing—original draft preparation, P.-F.Y.; writing—review and editing, S.-Q.Y. and P.G.R.; supervision, S.-Q.Y. and P.G.R.; funding acquisition, P.-F.Y. and S.-Q.Y. All authors have read and agreed to the published version of the manuscript.

Funding: This research was supported by the National Natural Science Foundation of China (NO. 42202300, NO. 42077231), the Basic Research Program of Jiangsu Province (Natural Science Foundation) for Youth Foundation (NO. BK20221150), and the Fundamental Research Funds for the Central Universities-Special Funds for the State Key Laboratory (NO. Z21003).

Conflicts of Interest: The authors declare no conflicts of interests.

References

1. Wang, Y.; Zhang, D.; Hu, Y.Z. Laboratory investigation of the effect of injection rate on hydraulic fracturing performance in artificial transversely laminated rock using 3D laser scanning. *Geotech. Geol. Eng.* **2019**, *37*, 2121–2133. [[CrossRef](#)]
2. Yang, S.Q.; Yin, P.F.; Ranjith, P.G. Experimental study on mechanical behavior and brittleness characteristics of Longmaxi formation shale in Changning, Sichuan basin, China. *Rock Mech. Rock Eng.* **2020**, *53*, 2461–2483. [[CrossRef](#)]
3. Saldungaray, P.; Palisch, T.T. Hydraulic fracture optimization in unconventional reservoirs. In Proceedings of the Society of Petroleum Engineers—SPE Middle East Unconventional Gas Conference and Exhibition, UGAS—Unlocking Unconventional Gas: New Energy in the Middle East, Abu Dhabi, United Arab Emirates, 23–25 January 2012; SPE-151128-MS.
4. Nguyen, V.P.; Lian, H.; Rabczuk, T.; Bordas, S. Modelling hydraulic fractures in porous media using flow cohesive interface elements. *Eng. Geol.* **2017**, *225*, 68–82. [[CrossRef](#)]
5. Taghichian, A.; Hashemalhosseini, H.; Zaman, M.; Yang, Z.Y. Geomechanical optimization of hydraulic fracturing in unconventional reservoirs: A semi-analytical approach. *Int. J. Fract.* **2018**, *213*, 107–138. [[CrossRef](#)]
6. Jain, R. Natural resource development for science, technology, and environmental policy issues: The case of hydraulic fracturing. *Clean Technol. Environ. Policy* **2015**, *17*, 3–8. [[CrossRef](#)]
7. Guo, C.H.; Xu, J.C.; Wei, M.Z.; Jiang, R.Z. Experimental Study and Numerical Simulation of Hydraulic Fracturing Tight Sandstone Reservoirs. *Fuel* **2015**, *159*, 334–344. [[CrossRef](#)]
8. Ibanez, W.D.; Kronenberg, A.K. Experimental deformation of shale: Mechanical properties and microstructural indicators of mechanisms. *Int. J. Rock Mech. Min. Sci. Geomech. Abstr.* **1993**, *30*, 723–734. [[CrossRef](#)]
9. Horsrud, P.; Sjonstebo, E.F.; Boe, R. Mechanical and petrophysical properties of North Sea shales. *Int. J. Rock Mech. Min. Sci.* **1998**, *35*, 1009–1020. [[CrossRef](#)]
10. Al-Bazali, T.; Zhang, J.G.; Chenevert, M.E.; Sharm, M.M. Factors controlling the compressive strength and acoustic properties of shale when interacting with water-based fluids. *Int. J. Rock Mech. Min. Sci.* **2008**, *45*, 729–738. [[CrossRef](#)]
11. Fjaer, E.; Nes, O.M. The Impact of Heterogeneity on the Anisotropic Strength of an Outcrop Shale. *Rock Mech. Rock Eng.* **2014**, *47*, 1603–1611. [[CrossRef](#)]
12. Holt, R.M.; Larsen, I.; Fjaer, E.; Stenebraten, J.F. Comparing mechanical and ultrasonic behaviour of a brittle and a ductile shale: Relevance to prediction of borehole stability and verification of shale barriers. *J. Pet. Sci. Eng.* **2020**, *187*, 106746. [[CrossRef](#)]
13. Gao, Q.; Tao, J.L.; Hu, J.Y.; Yu, X. Laboratory study on the mechanical behaviors of an anisotropic shale rock. *J. Rock Mech. Geotech. Eng.* **2015**, *7*, 213–219. [[CrossRef](#)]
14. Amadei, B. Importance of anisotropy when estimating and measuring in situ stresses in rock. *Int. J. Rock Mech. Min. Sci.* **1996**, *33*, 293–325. [[CrossRef](#)]
15. Chen, C.; Pan, E.; Amadei, B. Determination of deformability and tensile strength of anisotropic rock using Brazilian tests. *Int. J. Rock Mech. Min. Sci.* **1998**, *35*, 43–61. [[CrossRef](#)]
16. Gale, J.F.W.; Reed, R.M.; Holder, J. Natural fractures in the Barnett Shale and their importance for hydraulic fracture treatments. *AAPG Bull.* **2007**, *91*, 603–622. [[CrossRef](#)]
17. Gale, J.F.W.; Laubach, S.E.; Olson, J.E.; Eichhuble, P.; Fall, A. Natural Fractures in shale: A review and new observations. *AAPG Bull.* **2014**, *98*, 2165–2216. [[CrossRef](#)]
18. Jones, L.E.A.; Wang, H.F. Ultrasonic velocities in Cretaceous shales from the Williston Basin. *Geophysics* **1981**, *46*, 288–297. [[CrossRef](#)]
19. Johnston, J.E.; Christensen, N.I. Seismic anisotropy of shales. *J. Geophys. Res. Solid Earth* **1995**, *100*, 5991–6003. [[CrossRef](#)]
20. Hornby, B.E. Experimental laboratory determination of the dynamic elastic properties of wet, drained shales. *J. Geophys. Res. Solid Earth* **1998**, *103*, 29945–29964. [[CrossRef](#)]
21. Hornby, B.E.; Schwartz, L.M.; Hudson, J.A. Anisotropic effective-medium modeling of the elastic properties of shales. *Geophysics* **1994**, *59*, 1570–1583. [[CrossRef](#)]
22. Holt, R.M.; Fjær, E.; Raaen, A.M.; Ringstad, C. Influence of stress state and stress history on acoustic wave propagation in sedimentary rocks. In *Shear Waves in Marine Sediments*; Springer: Dordrecht, The Netherlands, 1991; pp. 167–174.
23. Sayers, C.M. Stress-dependent seismic anisotropy of shales. *Geophysics* **1999**, *64*, 93–98. [[CrossRef](#)]
24. Vernik, L.; Landis, C. Elastic anisotropy of source rocks: Implications for hydrocarbon generation and primary migration. *AAPG Bull.* **1996**, *80*, 531–544.
25. Jin, Z.F.; Li, W.X.; Jin, C.R.; Hambleton, J.; Cusatis, G. Elastic, strength, and fracture properties of Marcellus shale. *Int. J. Rock Mech. Min. Sci.* **2018**, *109*, 124–137. [[CrossRef](#)]
26. Loucks, R.G.; Reed, R.M.; Ruppel, S.C.; Hammes, U. Spectrum of pore types and networks in mudrocks and a descriptive classification for matrix-related mudrock pores. *AAPG Bull.* **2012**, *96*, 1071–1098. [[CrossRef](#)]

27. Sone, H.; Zoback, M.D. Mechanical properties of shale-gas reservoir rocks—Part 1: Static and dynamic elastic properties and anisotropy. *Geophysics* **2013**, *78*, 381–392. [[CrossRef](#)]
28. Revil, A.; Grauls, D.; Brevart, O. Mechanical compaction of sand/clay mixtures. *J. Geophys. Res.* **2002**, *107*, 2293. [[CrossRef](#)]
29. Crawford, B.R.; Faulkner, D.R.; Rutter, E.H. Strength, porosity, and permeability development during hydrostatic and shear loading of synthetic quartz-clay fault gouge. *J. Geophys. Res. Solid Earth* **2008**, *113*, B03207. [[CrossRef](#)]
30. Kohli, A.H.; Zoback, M.D. Frictional properties of shale reservoir rocks. *J. Geophys. Res. Solid Earth* **2013**, *118*, 5109–5125. [[CrossRef](#)]
31. Bai, B.J.; Elgmati, M.; Zhang, H.; Wei, M.Z. Rock characterization of Fayetteville shale gas plays. *Fuel* **2013**, *105*, 645–652. [[CrossRef](#)]
32. Wang, J.X.; Xie, L.Z.; Xie, H.P.; Ren, L.; He, B.; Li, C.B.; Yang, Z.P.; Gao, C. Effect of layer orientation on acoustic emission characteristics of anisotropic shale in Brazilian tests. *J. Nat. Gas Sci. Eng.* **2016**, *36*, 1120–1129. [[CrossRef](#)]
33. Hou, P.; Gao, F.; Yang, Y.G.; Zhang, Z.Z.; Zhang, X.X. Effect of bedding orientation on failure of black shale under Brazilian tests and energy analysis. *Chin. J. Geotech. Eng.* **2016**, *38*, 930–937.
34. Li, C.B.; Gao, C.; Xie, H.P.; Li, N. Experimental investigation of anisotropic fatigue characteristics of shale under uniaxial cyclic loading. *Int. J. Rock Mech. Min. Sci.* **2020**, *130*, 104314. [[CrossRef](#)]
35. Li, C.B.; Wang, J.; Xie, H.P. Anisotropic creep characteristics and mechanism of shale under elevated deviatoric stress. *J. Pet. Sci. Eng.* **2020**, *185*, 106670. [[CrossRef](#)]
36. Heng, S.; Yang, C.H.; Zhang, B.P.; Guo, Y.T.; Wang, L.; Wei, Y.L. Experimental research on anisotropic properties of shale. *Chin. J. Rock Soil Mech.* **2015**, *36*, 609–616.
37. Luo, Y.; Xie, H.P.; Ren, L.; Zhang, R.; Li, C.B.; Gao, C. Linear elastic fracture mechanics characterization of an anisotropic shale. *Sci. Rep.* **2018**, *8*, 8505. [[CrossRef](#)] [[PubMed](#)]
38. Zou, Y.S.; Zhang, S.C.; Zhou, T.; Zhou, X.; Guo, T.K. Experimental investigation into hydraulic fracture network propagation in gas shales using CT scanning technology. *Rock Mech. Rock Eng.* **2016**, *49*, 33–45.
39. Guo, T.K.; Zhang, S.C.; Qu, Z.Q.; Zhou, T.; Xiao, Y.S.; Gao, J. Experimental study of hydraulic fracturing for shale by stimulated reservoir volume. *Fuel* **2014**, *128*, 373–380. [[CrossRef](#)]
40. Lin, C.; He, J.M.; Li, X.; Wan, X.L.; Zheng, B. An experimental investigation into the effects of the anisotropy of shale on hydraulic fracture propagation. *Rock Mech. Rock Eng.* **2017**, *50*, 543–554. [[CrossRef](#)]
41. Masri, M.; Sibai, M.; Shao, J.F.; Mainguy, M. Experimental investigation of the effect of temperature on the mechanical behavior of Tournemire shale. *Int. J. Rock Mech. Min. Sci.* **2014**, *70*, 185–191. [[CrossRef](#)]
42. Rybacki, E.; Reinicke, A.; Meier, T.; Makasi, M.; Dresen, G. What controls the mechanical properties of shale rocks?—Part I: Strength and young’s modulus. *J. Pet. Sci. Eng.* **2015**, *135*, 702–722. [[CrossRef](#)]
43. Rybacki, E.; Meier, T.; Dresen, G. What controls the mechanical properties of shale rocks?—Part II: Brittleness. *J. Pet. Sci. Eng.* **2016**, *144*, 39–58. [[CrossRef](#)]
44. Mokhtari, M.; Alqahtani, A.A.; Tutuncu, A.N. Failure Behavior of Anisotropic Shales. In Proceedings of the 47th US Rock Mechanics/Geomechanics Symposium, San Francisco, CA, USA, 23–26 June 2013.
45. Heng, S.; Yang, C.H.; Guo, Y.T.; Wang, C.Y.; Wang, L. Influence of bedding planes on hydraulic fracture propagation in shale formations. *Chin. J. Rock Mech. Eng.* **2015**, *34*, 228–237.
46. Heng, S.; Guo, Y.T.; Yang, C.H.; Daemen, J.J.K.; Li, Z. Experimental and theoretical study of the anisotropic properties of shale. *Int. J. Rock Mech. Min. Sci.* **2015**, *74*, 58–68. [[CrossRef](#)]
47. Jarvie, D.M.; Hill, R.J.; Ruble, T.E.; Pollastro, R.M. Unconventional shale-gas systems: The Mississippian Barnett shale of north-central Texas as one model for thermogenic shale-gas assessment. *AAPG Bull.* **2007**, *91*, 475–499. [[CrossRef](#)]
48. Li, Q.H.; Chen, M.; Jin, Y.; Wang, F.P.; Hou, B.; Zhang, B. Indoor evaluation method for shale brittleness and improvement. *Chin. J. Rock Mech. Eng.* **2012**, *31*, 1680–1685.
49. Kivi, I.R.; Ameri, M.; Molladavoodi, H. Shale brittleness evaluation based on energy balance analysis of stress-strain curves. *J. Pet. Sci. Eng.* **2018**, *167*, 1–19. [[CrossRef](#)]
50. Qian, K.R.; Liu, T.; Liu, J.Z.; Liu, X.W.; He, Z.L.; Jiang, D.J. Construction of a novel brittleness index equation and analysis of anisotropic brittleness characteristics for unconventional shale formations. *Pet. Sci.* **2020**, *17*, 70–85. [[CrossRef](#)]
51. Huang, X.R.; Huang, J.P.; Li, Z.C.; Yang, Q.Y.; Sun, Q.X.; Cui, W. Brittleness index and seismic rock physics model for anisotropic tight-oil sandstone reservoirs. *Appl. Geophys.* **2015**, *12*, 11–22. [[CrossRef](#)]
52. Schmidt, R.A.; Huddle, C.W. *Fracture Mechanics of Oil Shale: Some Preliminary Results*; Report No. SAND-76-0727; Sandia Labs: Albuquerque, NM, USA, 1997; 29p. [[CrossRef](#)]
53. Lee, H.P.; Olson, J.E.; Holder, J.; Gale, J.F.W.; Myers, R.D. The interaction of propagating opening mode fractures with preexisting discontinuities in shale. *J. Geophys. Res. Solid Earth* **2015**, *120*, 169–181. [[CrossRef](#)]
54. Chandler, M.R.; Meredith, P.G.; Brantut, N.; Crawford, B.R. Fracture toughness anisotropy in shale. *J. Geophys. Res. Solid Earth* **2016**, *121*, 1706–1729. [[CrossRef](#)]
55. Yin, S.; Lv, D.W.; Jin, L.; Ding, W.L. Experimental analysis and application of the effect of stress on continental shale reservoir brittleness. *J. Geophys. Eng.* **2018**, *15*, 478–494. [[CrossRef](#)]
56. Zhao, Y.; He, P.F.; Zhang, Y.F.; Wang, C.L. A new criterion for a toughness-dominated hydraulic fracture crossing a natural frictional interface. *Rock Mech. Rock Eng.* **2019**, *52*, 2617–2629. [[CrossRef](#)]

57. Zhao, Y.; Zhang, Y.F.; He, P.F. A composite criterion to predict subsequent intersection behavior between a hydraulic fracture and a natural fracture. *Eng. Fract. Mech.* **2019**, *209*, 61–78. [[CrossRef](#)]
58. Kou, M.M.; Liu, X.R.; Tang, S.D.; Wang, Y.T. 3-D X-ray computed tomography on failure characteristics of rock-like materials under coupled hydro-mechanical loading. *Theor. Appl. Fract. Mech.* **2019**, *104*, 102396. [[CrossRef](#)]
59. Kou, M.M.; Liu, X.R.; Wang, Y.T. Study on rock fracture behavior under hydromechanical loading by 3-D digital reconstruction. *Struct. Eng. Mech.* **2020**, *74*, 283–296.
60. Zhang, Y.F.; Zhao, Y.; Yang, H.Q.; Wang, C.L. A semianalytical solution for a Griffith crack nonuniformly pressurized by internal fluid. *Rock Mech. Rock Eng.* **2020**, *53*, 2439–2460. [[CrossRef](#)]
61. Zhao, Y.; Zhang, Y.F.; Wang, C.L.; Liu, Q. Hydraulic fracturing characteristics and evaluation of fracturing effectiveness under different anisotropic angles and injection rates: An experimental investigation in absence of confining pressure. *J. Nat. Gas Sci. Eng.* **2022**, *97*, 104343. [[CrossRef](#)]
62. Yaalon, D.H. Mineral composition of average shale. *Clay Min. Bull.* **1962**, *5*, 31–36. [[CrossRef](#)]
63. Sliwinski, J.; Harrington, J.; Power, M.; Hughes, P.; Yeung, B. A high definition mineralogical examination of potential gas shales. Abstract Volume. In Proceedings of the AAPG—Annual Convention and Exhibition, New Orleans, LA, USA, 11–14 April 2010; p. 239.
64. Lyu, Q.; Shi, J.D.; Ranjith, P.G. Effects of testing method, lithology and fluid-rock interactions on shale permeability: A review of laboratory measurements. *J. Nat. Gas Sci. Eng.* **2020**, *78*, 1033023. [[CrossRef](#)]
65. Minaeian, V.; Dewhurst, D.N.; Rasouli, V. Deformational behaviour of a clay-rich shale with variable water saturation under true triaxial stress conditions. *Geomech. Energy Environ.* **2017**, *11*, 1–13. [[CrossRef](#)]
66. Wu, C.J.; Tuo, J.C.; Zhang, L.F.; Zhang, M.F.; Li, J.; Liu, Y.; Qian, Y. Pore characteristics differences between clay-rich and clay-poor shales of the Lower Cambrian Niutitang Formation in the Northern Guizhou area, and insights into shale gas storage mechanisms. *Int. J. Coal Geol.* **2017**, *178*, 13–25. [[CrossRef](#)]
67. Zhang, J.J.; Kamenov, A.; Zhu, D.; Hill, A.D. Development of new testing procedures to measure propped fracture conductivity considering water damage in clay-rich shale reservoirs: An example of the Barnett Shale. *J. Pet. Sci. Eng.* **2015**, *135*, 352–359. [[CrossRef](#)]
68. Amalokwu, K.; Spikes, K.; Wolf, K. A simple effective medium approach for the bulk electrical and elastic properties of organic-rich shales. *J. Appl. Geophys.* **2019**, *169*, 98–108. [[CrossRef](#)]
69. Wang, Y.P.; Liu, X.J.; Liang, L.X.; Xiong, J. Experimental study on the damage of organic-rich shale during water-shale interaction. *J. Nat. Gas Sci. Eng.* **2020**, *74*, 103103. [[CrossRef](#)]
70. Wei, M.M.; Zhang, L.; Xiong, Y.Q.; Peng, P.A. Main factors influencing the development of nanopores in over-mature, organic-rich shales. *Int. J. Coal Geol.* **2019**, *212*, 103233. [[CrossRef](#)]
71. Ilgen, A.G.; Aman, M.; Espinoza, D.N.; Rodriguez, M.A.; Griego, J.M.; Dewers, T.A.; Feldman, J.D.; Stewart, T.A.; Choens, R.C.; Wilson, J. Shale-brine-CO₂ interactions and the long-term stability of carbonate-rich shale caprock. *Int. J. Greenh. Gas Control* **2018**, *78*, 244–253. [[CrossRef](#)]
72. Teklu, T.W.; Abass, H.H.; Hanashmoon, R.; Carratu, J.C.; Ermila, M. Experimental investigation of acid imbibition on matrix and fractured carbonate rich shales. *J. Nat. Gas Sci. Eng.* **2017**, *45*, 706–725. [[CrossRef](#)]
73. Rickman, R.; Mullen, M.J.; Petre, J.E.; Grieser, W.V.; Kundert, D. A practical use of shale petrophysics for stimulation design optimization: All shale plays are not clones of the Barnett shale. In Proceedings of the SPE Annual Technical Conference and Exhibition, Society of Petroleum Engineers, Denver, CO, USA, 21–24 September 2008.
74. Civan, F. *Reservoir Formation Damage*; Gulf Publishing Company: Houston, TX, USA, 2007.
75. Loucks, R.G.; Ruppel, S.C. Mississippian Barnett Shale: Lithofacies and depositional setting of a deep-water shale-gas succession in the Fort Worth Basin, Texas. *AAPG Bull.* **2007**, *91*, 579–601. [[CrossRef](#)]
76. Li, G.F.; Jin, Z.J.; Li, X.; Liu, K.Q.; Yang, W.C.; Qiao, M.T.; Zhou, T.T.; Sun, X.K. Experimental study on mechanical properties and fracture characteristics of shale layered samples with different mineral components under cyclic loading. *Mar. Pet. Geol.* **2023**, *150*, 106114. [[CrossRef](#)]
77. Wang, Y.; Li, C.H. Investigation of the p- and s-wave velocity anisotropy of a Longmaxi formation shale by real-time ultrasonic and mechanical experiments under uniaxial deformation. *J. Pet. Sci. Eng.* **2017**, *158*, 253–267. [[CrossRef](#)]
78. Niandou, H.; Shao, J.F.; Henry, J.P.; Fourmaintraux, D. Laboratory investigation of the mechanical behaviour of Tournemire shale. *Int. J. Rock Mech. Min. Sci.* **1997**, *34*, 3–16. [[CrossRef](#)]
79. Jia, Y.Z.; Tang, J.R.; Lu, Y.Y.; Lu, Z.H. Laboratory geomechanical and petrophysical characterization of Longmaxi shale properties in Lower Silurian Formation, China. *Mar. Pet. Geol.* **2020**, *124*, 104800. [[CrossRef](#)]
80. Liu, Y.; Ma, T.; Wu, H.; Chen, P. Investigation on mechanical behaviors of shale cap rock for geological energy storage by linking macroscopic to mesoscopic failures. *J. Energy Storage* **2020**, *29*, 101326. [[CrossRef](#)]
81. Yang, S.Q.; Yin, P.F.; Li, B.; Yang, D.S. Behavior of transversely isotropic shale observed in triaxial tests and Brazilian disc tests. *Int. J. Rock Mech. Min. Sci.* **2020**, *133*, 104435. [[CrossRef](#)]
82. Brahma, J.; Sircar, A. Estimation of the effect of anisotropy on Young's moduli and Poisson's ratios of sedimentary rocks using core samples in western and central part of Tripura, India. *Int. J. Geosci.* **2014**, *05*, 184–195. [[CrossRef](#)]
83. Lo, T.W.; Coyner, K.B.; Toksoz, M.N. Experimental determination of elastic anisotropy of Berea sandstone, Chicopee shale, and Chelmsford granite. *Geophysics* **1986**, *51*, 164–171. [[CrossRef](#)]

84. Allan, A.M.; Kanitpanyacharoen, W.; Vanorio, T. A multiscale methodology for the analysis of velocity anisotropy in organic-rich shale. *Geophysics* **2015**, *80*, 73–88. [[CrossRef](#)]
85. Alejano, L.R.; González-Fernández, M.A.; Estévez-Ventosa, X.; Song, F.; Delgado-Martín, J.; Muoz-Ibáez, A.; Gonzalez-Molano, N.; Alvarellos, J. Anisotropic deformability and strength of slate from NW-Spain. *Int. J. Rock Mech. Min. Sci.* **2021**, *148*, 104923. [[CrossRef](#)]
86. Hou, Z.K.; Yang, C.H.; Guo, Y.T.; Zhang, B.P.; Wei, Y.L.; Heng, S.; Wang, L. Experimental study on anisotropic properties of Longmaxi formation shale under uniaxial compression. *Chin. J. Rock Soil Mech.* **2015**, *36*, 2541–2550.
87. Dewhurst, D.N.; Siggins, A.F.; Sarout, J.; Raven, M.D.; Nordgård-Bolås, H.M. Geomechanical and ultrasonic characterization of a Norwegian Sea shale. *Geophysics* **2011**, *76*, 101–111. [[CrossRef](#)]
88. Zhubayev, A.; Houben, M.E.; Smeulders, D.M.J.; Barnhoorn, A. Ultrasonic velocity and attenuation anisotropy of shales, Whitby, United Kingdom. *Geophysics* **2015**, *81*, 45–56. [[CrossRef](#)]
89. Jin, G.; Ali, S.S.; Abdullah, A.; Dhamen, A. Mechanical anisotropy of unconventional shale—Build the correct relationship between static and dynamic properties. In Proceedings of the 2016 Abu Dhabi International Petroleum Exhibition & Conference, Society of Petroleum Engineers, Abu Dhabi, United Arab Emirates, 7–10 November 2016; pp. 1–9.
90. Iferobia, C.C.; Ahmad, M. A review on the experimental techniques and applications in the geomechanical evaluation of shale gas reservoirs. *J. Nat. Gas Sci. Eng.* **2020**, *74*, 103090. [[CrossRef](#)]
91. Rasouli, V. Geomechanics of gas shales. In *Fundamentals of Gas Shale Reservoirs*; Rezaee, R., Ed.; John Wiley & Sons, Inc.: Hoboken, NJ, USA, 2015; pp. 169–190.
92. Panfiloff, A. *Experimental Evaluation of Dynamic Elastic Properties and Anisotropy in Shales*; Colorado School of Mines: Golden, CO, USA, 2016.
93. Yin, P.F.; Yang, S.Q. Experimental study on strength and failure behavior of transversely isotropic rock-like material under uniaxial compression. *Geomech. Geophys. Geo-Energy Geo-Resour.* **2020**, *6*, 44. [[CrossRef](#)]
94. Kuila, U.; Dewhurst, D.N.; Siggins, A.F.; Raven, M.D. Stress anisotropy and velocity anisotropy in low porosity shale. *Tectonophysics* **2011**, *50*, 34–44. [[CrossRef](#)]
95. Cho, J.W.; Kim, H.; Jeon, S.; Min, K.B. Deformation and strength anisotropy of Asan gneiss, Boryeong shale, and Yeoncheon schist. *Int. J. Rock Mech. Min. Sci.* **2012**, *50*, 158–169. [[CrossRef](#)]
96. Kim, H.; Cho, J.W.; Song, I.; Min, K.B. Anisotropy of elastic moduli, p-wave velocities, and thermal conductivities of Asan gneiss, Boryeong shale, and Yeoncheon schist in Korea. *Eng. Geol.* **2012**, *147–148*, 68–77. [[CrossRef](#)]
97. Yang, S.Q.; Yin, P.F.; Huang, Y.H. Experiment and discrete element modelling on strength, deformation and failure behaviour of shale under Brazilian compression. *Rock Mech. Rock Eng.* **2019**, *52*, 4339–4359. [[CrossRef](#)]
98. Josh, M.; Esteban, L.; Piane, C.D.; Sarout, J.; Dewhurst, D.N.; Clennell, M.B. Laboratory characterisation of shale properties. *J. Pet. Sci. Eng.* **2012**, *88–89*, 107–124. [[CrossRef](#)]
99. Wu, S.; Ge, H.K.; Wang, X.Q.; Meng, F.B. Shale failure processes and spatial distribution of fractures obtained by AE monitoring. *J. Nat. Gas Sci. Eng.* **2017**, *41*, 82–92. [[CrossRef](#)]
100. Li, X.L.; Lei, X.; Li, Q.; Li, X. Experimental investigation of Sinian shale rock under triaxial stress monitored by ultrasonic transmission and acoustic emission. *J. Nat. Gas Sci. Eng.* **2017**, *43*, 110–123. [[CrossRef](#)]
101. Nasser, M.H.; Rao, K.S.; Ramamurthy, T. Failure mechanism in schistose rocks. *Int. J. Rock Mech. Min. Sci.* **1997**, *34*, 219. [[CrossRef](#)]
102. Nasser, M.H.; Rao, K.S.; Ramamurthy, T. Anisotropic strength and deformational behavior of Himalayan schists. *Int. J. Rock Mech. Min. Sci.* **2003**, *40*, 3–23. [[CrossRef](#)]
103. Hakala, M.; Kuula, H.; Hudson, J.A. Estimating the transversely isotropic elastic intact rock properties for in situ stress measurement data reduction: A case study of the Olkiluoto mica gneiss, Finland. *Int. J. Rock Mech. Min. Sci.* **2007**, *44*, 14–46. [[CrossRef](#)]
104. Yin, P.F.; Yang, S.Q. Experimental investigation of the strength and failure behavior of layered sandstone under uniaxial compression and Brazilian testing. *Acta Geophys.* **2018**, *66*, 585–605. [[CrossRef](#)]
105. Ramamurthy, T. Strength, modulus responses of anisotropic rocks. In *Compressive Rock Engineering*; Hudson, J.A., Ed.; Pergamon: Oxford, UK, 1993; Volume 1, pp. 313–329.
106. Gao, C.; Xie, L.Z.; Xie, H.P.; He, B.; Jin, W.C.; Li, F.; Yang, Z.P.; Sun, Y.Z. Estimation of the equivalent elastic modulus in shale formation: Theoretical model and experiment. *J. Pet. Sci. Eng.* **2017**, *151*, 468–479. [[CrossRef](#)]
107. Zuo, J.P.; Lu, J.F.; Ghandriz, R.; Wang, J.T.; Li, Y.H.; Zhang, X.Y.; Li, J.; Li, H.T. Mesoscale fracture behavior of Longmaxi outcrop shale with different bedding angles: Experimental and numerical investigations. *J. Rock Mech. Geotech. Eng.* **2020**, *12*, 297–309. [[CrossRef](#)]
108. Hu, J.J.; Gao, C.; Xie, H.P.; Wang, J.; Li, M.H.; Li, C.B. Anisotropic characteristics of the energy index during the shale failure process under triaxial compression. *J. Nat. Gas Sci. Eng.* **2021**, *95*, 104219. [[CrossRef](#)]
109. Jaeger, J.C. Shear failure of transversely isotropic rock. *Geol. Mag.* **1960**, *97*, 65–72. [[CrossRef](#)]
110. Hoek, E.; Brown, E.T. *Underground Excavations in Rock*; Institution of Mining and Metallurgy: London, UK, 1980.
111. Rao, K.S.; Rao, G.V.; Ramamurthy, T. A strength criterion for anisotropic rocks. *Indian Geotech. J.* **1986**, *16*, 317–333.
112. Ramamurthy, T.; Rao, G.V.; Singh, J. A strength criterion for anisotropic rocks. In Proceedings of the Fifth Australia–New Zealand Conference on Geomechanics, Sydney, Australia, 22–26 August 1988; Volume 1, pp. 253–257.

113. Tien, Y.M.; Kuo, M.C. A failure criterion for transversely isotropic rocks. *Int. J. Rock Mech. Min. Sci.* **2001**, *38*, 399–412. [[CrossRef](#)]
114. Saeidi, O.; Vaneghi, R.G.; Rasouli, V.; Gholami, R. A modified empirical criterion for strength of transversely anisotropic rocks with metamorphic origin. *Bull. Eng. Geol. Environ.* **2013**, *72*, 257–269. [[CrossRef](#)]
115. Saeidi, O.; Vaneghi, R.G.; Rasouli, V.; Gholami, R.; Torabi, S.R. A modified failure criterion for transversely isotropic rocks. *Geosci. Front.* **2014**, *5*, 215–225. [[CrossRef](#)]
116. Singh, M.; Samadhiya, N.K.; Kumar, A. A nonlinear criterion for triaxial strength of inherently anisotropic rocks. *Rock Mech. Rock Eng.* **2015**, *48*, 1387–1405. [[CrossRef](#)]
117. Shi, X.C.; Yang, X.; Meng, X.F. An anisotropic strength model for layered rocks considering planes of weakness. *Rock Mech. Rock Eng.* **2016**, *49*, 3783–3792. [[CrossRef](#)]
118. Rafiai, H. New empirical polyaxial criterion for rock strength. *Int. J. Rock Mech. Min. Sci.* **2011**, *48*, 922–931. [[CrossRef](#)]
119. Chen, L.; Shao, J.F.; Huang, H.W. Coupled elastoplastic damage modeling of anisotropic rocks. *Comput. Geotech.* **2010**, *37*, 187–194. [[CrossRef](#)]
120. Chen, L.; Shao, J.F.; Zhu, Q.Z.; Duveau, G. Induced anisotropic damage and plasticity in initially anisotropic sedimentary rocks. *Int. J. Rock Mech. Min. Sci.* **2012**, *51*, 13–23. [[CrossRef](#)]
121. Yao, C.; Jiang, Q.H.; Shao, J.F.; Zhou, C.B. A discrete approach for modeling damage and failure in anisotropic cohesive brittle materials. *Eng. Fract. Mech.* **2016**, *155*, 102–118. [[CrossRef](#)]
122. Qi, M.; Giraud, A.; Colliat, J.B.; Shao, J.F. A numerical damage model for initially anisotropic materials. *Int. J. Solids Struct.* **2016**, *100–101*, 245–256. [[CrossRef](#)]
123. Qi, M.; Shao, J.F.; Giraud, A.; Zhu, Q.Z.; Colliat, J.B. Damage and plastic friction in initially anisotropic quasi brittle materials. *Int. J. Plast.* **2016**, *82*, 260–282. [[CrossRef](#)]
124. Tien, Y.M.; Kuo, M.C.; Juang, C.H. An experimental investigation of the failure mechanism of simulated transversely isotropic rocks. *Int. J. Rock Mech. Min. Sci.* **2006**, *43*, 1163–1181. [[CrossRef](#)]
125. Deng, J.X.; Shi, G.; Liu, R.X.; Yu, J. Analysis of the velocity anisotropy and its affection factors in shale and mudstone. *Chin. J. Geophys.* **2004**, *47*, 862–868.
126. Zhao, C.X.; Liu, J.F.; Xu, D.; Zhang, L.Q.; Lyu, C.; Ren, Y. Investigation on Mechanical Properties, AE Characteristics, and Failure Modes of Longmaxi Formation Shale in Changning, Sichuan Basin, China. *Rock Mech. Rock Eng.* **2023**, *56*, 1239–1272. [[CrossRef](#)]
127. Amadei, B.; Rogers, J.D.; Goodman, R.E. Elastic Constants and Tensile Strength of Anisotropic Rocks. In Proceedings of the 5th ISRM Congress, Melbourne, Australia, 10–15 April 1983; ISRM-5CONGRESS-1983-030.
128. Lekhnitskii, S.G. *Anisotropic Plates*; Gordon and Breach: New York, NY, USA, 1968.
129. Tavallali, A.; Vervoort, A. Failure of transversely isotropic rock material: Effect of layer orientation and material properties. In Proceedings of the 6th International Symposium on Ground Support in Mining and Civil Engineering Construction, Cape Town, South Africa, 30 March–3 April 2008; pp. 317–328.
130. Tavallali, A.; Vervoort, A. Failure of layered sandstone under Brazilian test conditions: Effect of micro-scale parameters on macro-scale behaviour. *Rock Mech. Rock Eng.* **2010**, *43*, 641–653. [[CrossRef](#)]
131. Tavallali, A.; Vervoort, A. Effect of layer orientation on the failure of layered sandstone under Brazilian test conditions. *Int. J. Rock Mech. Min. Sci.* **2010**, *47*, 313–322. [[CrossRef](#)]
132. Tavallali, A.; Vervoort, A. Behaviour of layered sandstone under Brazilian test conditions: Layer orientation and shape effects. *J. Rock Mech. Geotech. Eng.* **2013**, *5*, 366–377. [[CrossRef](#)]
133. Vervoort, A.; Min, K.B.; Konietzky, H.; Cho, J.W.; Debecker, B.; Din, Q.D.; Frühwirt, T.; Tavallali, A. Failure of transversely isotropic rock under Brazilian test conditions. *Int. J. Rock Mech. Min. Sci.* **2014**, *70*, 343–352. [[CrossRef](#)]
134. Tan, X.; Konietzky, H.; Frühwirt, T.; Dan, D.Q. Brazilian tests on transversely isotropic rocks: Laboratory testing and numerical simulations. *Rock Mech. Rock Eng.* **2015**, *48*, 1341–1351. [[CrossRef](#)]
135. Yang, Z.P.; He, B.; Xie, L.Z.; Li, C.B.; Wang, J. Strength and failure modes of shale based on Brazilian test. *Chin. J. Rock Soil Mech.* **2015**, *36*, 3447–3464.
136. Hou, P.; Gao, F.; Yang, Y.G.; Zhang, Z.Z.; Gao, Y.N.; Zhang, X.X.; Zhang, J. Effect of bedding plane direction on acoustic emission characteristics of shale in Brazilian tests. *Chin. J. Rock Soil Mech.* **2016**, *37*, 1603–1612.
137. Du, M.P.; Pan, P.Z.; Ji, W.W.; Zhang, Z.H.; Gao, Y.H. Time-space laws of failure process of carbonaceous shale in Brazilian split test. *Chin. J. Rock Soil Mech.* **2016**, *37*, 3437–3446.
138. He, J.; Afolagboye, L.O. Influence of layer orientation and interlayer bonding force on the mechanical behavior of shale under Brazilian test conditions. *Acta Mech. Sin.* **2018**, *34*, 349–358. [[CrossRef](#)]
139. Simpson, N.D.J.; Stroisz, A.; Bauer, A.; Vervoort, A.; Holt, R.M. Failure mechanics of anisotropic shale during Brazilian tests. In Proceedings of the 48th US Rock Mechanics/Geomechanics Symposium, Minneapolis, MN, USA, 1–4 June 2014; ARMA 14-7399.
140. Chandler, M.; Meredith, P.; Crawford, B. Experimental determination of the fracture toughness and brittleness of the Mancos shale. *Utah Br. J. Psychiatry* **2013**, *184*, 110–117.
141. Chen, M.; Zhang, G.Q. Laboratory measurement and interpretation of the fracture toughness of formation rocks at great depth. *J. Pet. Sci. Eng.* **2004**, *41*, 221–231. [[CrossRef](#)]
142. Awaji, H.; Sato, S. Combined mode fracture toughness measurement by the disk test. *J. Eng. Mater. Technol.* **1978**, *100*, 175–182. [[CrossRef](#)]

143. Atkinson, C.; Smelser, R.E.; Sanchez, J. Combined mode fracture via the cracked Brazilian disk test. *Int. J. Fract.* **1982**, *18*, 279–291. [[CrossRef](#)]
144. Chong, K.P.; Kuruppu, M.D. New specimen for fracture toughness determination for rock and other materials. *Int. J. Fract.* **1984**, *26*, 59–62. [[CrossRef](#)]
145. Lim, I.L.; Johnston, I.W.; Choi, S.K.; Boland, J.N. Fracture testing of a soft rock with semi-circular specimens under three-point bending. Part 2—Mixed-mode. *Int. J. Rock Mech. Min. Sci.* **1994**, *31*, 199–212. [[CrossRef](#)]
146. Dai, F.; Chen, R.; Xia, K. A semi-circular bend technique for determining dynamic fracture toughness. *Exp. Mech.* **2010**, *50*, 783–791. [[CrossRef](#)]
147. Funatsu, T.; Shimizu, N.; Kuruppu, M.; Matsui, K. Evaluation of mode I fracture toughness assisted by the numerical determination of K-resistance. *Rock Mech. Rock Eng.* **2014**, *48*, 143–157. [[CrossRef](#)]
148. Ren, L.; Xie, L.Z.; Xie, H.P.; Ai, T.; He, B. Mixed-mode fracture behavior and related surface topography feature of a typical sandstone. *Rock Mech. Rock Eng.* **2016**, *49*, 3137–3153. [[CrossRef](#)]
149. *ASTM E399–12e3*; Standard Test Method for Linear-Elastic Plane-Strain Fracture Toughness K_{IC} of Metallic Materials. ASTM International: West Conshohocken, PA, USA, 2009.
150. Bush, A.J. Experimentally determined stress-intensity factors for single-edge-crack round bars loaded in bending. *Exp. Mech.* **1976**, *16*, 249–257. [[CrossRef](#)]
151. Luo, Y.; Ren, L.; Xie, L.Z.; Ai, T.; He, B. Fracture behavior investigation of a typical sandstone under mixed-mode I/II loading using the notched deep beam bending method. *Rock Mech. Rock Eng.* **2017**, *50*, 1987–2005. [[CrossRef](#)]
152. Wu, S.X. Fracture toughness determination of bearing steel using chevron-notch three point bend specimen. *Eng. Fract. Mech.* **1984**, *19*, 221–232. [[CrossRef](#)]
153. Ren, L.; Xie, H.P.; Sun, X.; Zhang, R.; Li, C.B.; Xie, J.; Zhang, Z.T. Characterization of Anisotropic Fracture Properties of Silurian Longmaxi Shale. *Rock Mech. Rock Eng.* **2021**, *54*, 665–678. [[CrossRef](#)]
154. Sheity, D.K.; Rosenfield, A.R.; Duckworth, W.H. Fracture toughness of ceramics measured by a chevron-notch diametral-compression test. *J. Am. Ceram. Soc.* **1985**, *68*, C325–C327. [[CrossRef](#)]
155. Fowell, R.J. Suggested method for determining mode I fracture toughness using cracked chevron notched Brazilian disc (CCNBD) specimens. *Int. J. Rock Mech. Min. Sci.* **1995**, *32*, 57–64. [[CrossRef](#)]
156. Dai, F.; Wei, M.D.; Xu, N.W.; Ma, Y.; Yang, D.S. Numerical assessment of the progressive rock fracture mechanism of cracked chevron notched Brazilian disc specimens. *Rock Mech. Rock Eng.* **2014**, *48*, 463–479. [[CrossRef](#)]
157. Kuruppu, M.D. Fracture toughness measurement using chevron notched semi-circular bend specimen. *Int. J. Fract.* **1997**, *86*, L33–L38.
158. Dai, F.; Xia, K.; Zheng, H.; Wang, Y.X. Determination of dynamic rock Mode-I fracture parameters using cracked chevron notched semi-circular bend specimen. *Eng. Fract. Mech.* **2011**, *78*, 2633–2644. [[CrossRef](#)]
159. Barker, L.M. A simplified method for measuring plane strain fracture toughness. *Eng. Fract. Mech.* **1977**, *9*, 361–369. [[CrossRef](#)]
160. Ouchterlony, F. A Presentation of the ISRM Suggested Methods for Determining Fracture Toughness of Rock Material. In Proceedings of the 6th ISRM Congress, Montreal, QC, Canada, 30 August–3 September 1987.
161. Wang, Q.Z.; Xing, L. Determination of fracture toughness K_{IC} by using the flattened Brazilian disk specimen for rocks. *Eng. Fract. Mech.* **1999**, *64*, 193–201. [[CrossRef](#)]
162. Schmidt, R.A. Fracture Mechanics of Oil Shale—Unconfined Fracture Toughness, Stress Corrosion Cracking, and Tension Test Results. In Proceedings of the 18th U.S. Symposium on Rock Mechanics (USRMS), Golden, CO, USA, 22–24 June 1977.
163. Chandler, M.R.; Fauchille, A.L.; Kim, H.K.; Ma, L.; Mecklenburgh, J.; Rizzo, R.; Mostafavi, M.; Marussi, S.; Atwood, R.; May, S.; et al. Correlative optical and X-ray imaging of strain evolution during double-torsion fracture toughness measurements in shale. *J. Geophys. Res. Solid Earth* **2018**, *123*, 10517–10533. [[CrossRef](#)]
164. Xiong, J.; Liu, K.Y.; Liang, L.X.; Liu, X.J.; Zhang, C.Y. Investigation of influence factors of the fracture toughness of shale: A case study of the Longmaxi formation shale in Sichuan basin, China. *Geotech. Geol. Eng.* **2019**, *37*, 2927–2934. [[CrossRef](#)]
165. Wang, H.J.; Zhao, F.; Huang, Z.Q.; Yao, Y.M.; Yuan, G.X. Experimental study of mode-I fracture toughness for layered shale based on two ISRM-suggested methods. *Rock Mech. Rock Eng.* **2017**, *50*, 1933–1939. [[CrossRef](#)]
166. Dou, F.K.; Wang, J.G.; Zhang, X.X.; Wang, H.M. Effect of joint parameters on fracturing behavior of shale in notched three-point-bending test based on discrete element model. *Eng. Fract. Mech.* **2019**, *205*, 40–56. [[CrossRef](#)]
167. Li, W.X.; Jin, Z.F.; Cusatis, G. Size effect analysis for the characterization of marcellus shale quasi-brittle fracture properties. *Rock Mech. Rock Eng.* **2019**, *52*, 1–18. [[CrossRef](#)]
168. Inskip, F.N.D.; Meredith, P.G.; Chandler, M.R.; Gudmundsson, A. Fracture properties of Nash Point shale as a function of orientation to bedding. *J. Geophys. Res. Solid Earth* **2018**, *123*, 8428–8444. [[CrossRef](#)]
169. Lei, B.; Zuo, J.P.; Liu, H.Y.; Wang, J.T.; Xu, F.; Li, H.T. Experimental and numerical investigation on shale fracture behavior with different bedding properties. *Eng. Fract. Mech.* **2021**, *247*, 107639. [[CrossRef](#)]
170. Shi, X.S.; Zhao, Y.X.; Danesh, N.N.; Zhang, X.; Tang, T.W. Role of bedding plane in the relationship between Mode-I fracture toughness and tensile strength of shale. *Bull. Eng. Geol. Environ.* **2022**, *81*, 81. [[CrossRef](#)]
171. Zhang, Y.; Li, T.Y.; Xie, L.Z.; Yang, Z.P.; Li, R.Y. Shale lamina thickness study based on micro-scale image processing of thin sections. *J. Nat. Gas Sci. Eng.* **2017**, *46*, 817–829. [[CrossRef](#)]

172. Zhou, Q.; Xie, H.P.; Zhu, Z.M.; He, R.; Lu, H.J.; Fan, Z.D.; Nie, X.F.; Ren, L. Fracture Toughness Anisotropy in Shale Under Deep in Situ Stress Conditions. *Rock Mech. Rock Eng.* **2023**, *56*, 7535–7555. [[CrossRef](#)]
173. Zhang, D.C.; Ranjith, P.G.; Perera, M.S.A. The brittleness indices used in rock mechanics and their application in shale hydraulic fracturing: A review. *J. Pet. Sci. Eng.* **2016**, *143*, 158–170. [[CrossRef](#)]
174. Morley, A. *Strength of Materials: With 260 Diagrams and Numerous Examples*; Longmans, Green and Company: New York, NY, USA, 1944.
175. Hetényi, M. *Handbook of Experimental Stress Analysis*; Wiley: New York, NY, USA, 1950.
176. Obert, L.; Duvall, W.I. *Rock Mechanics and the Design of Structures in Rock*; Wiley: New York, NY, USA, 1967.
177. Ramsey, J. *Folding and Fracturing of Rock*; McGraw-Hill: New York, NY, USA, 1968.
178. Howell, J.V. *Glossary of Geology and Related Sciences*; American Geological Institute: Washington, DC, USA, 1960.
179. Tarasov, B.; Potvin, Y. Universal criteria for rock brittleness estimation under triaxial compression. *Int. J. Rock Mech. Min. Sci.* **2013**, *59*, 57–69. [[CrossRef](#)]
180. Hucka, V.; Das, B. Brittleness determination of rocks by different methods. *Int. J. Rock Mech. Min. Sci.* **1974**, *17*, 389–392. [[CrossRef](#)]
181. Altindag, R. The evaluation of rock brittleness concept on rotary blast hole drills. *J. South. Afr. Inst. Min. Metall.* **2002**, *102*, 61–66.
182. Hajiabdolmajid, V.; Kaiser, P.; Martin, C.D. Mobilised strength components in brittle failure of rock. *Géotechnique* **2003**, *53*, 327–336. [[CrossRef](#)]
183. Nygård, R.; Gutierrez, M.; Bratli, R.K.; Høeg, K. Brittle–ductile transition, shear failure and leakage in shales and mudrocks. *Mar. Pet. Geol.* **2006**, *23*, 201–212. [[CrossRef](#)]
184. Yagiz, S. Assessment of brittleness using rock strength and density with punch penetration test. *Tunn. Undergr. Space Technol.* **2009**, *24*, 66–74. [[CrossRef](#)]
185. Holt, R.M.; Fjaer, E.; Nes, O.M.; Alassi, H.T. A shaly look at brittleness. In Proceedings of the 45th US Rock Mechanics/Geomechanics Symposium, San Francisco, CA, USA, 26–29 June 2011. 10p.
186. Jin, X.; Shah, S.N.; Roegiers, J.C.; Zhang, B. Fracability evaluation in shale reservoirs—An integrated petrophysics and geomechanics approach. In Proceedings of the SPE Hydraulic Fracturing Technology Conference, The Woodlands, TX, USA, 4–6 February 2014.
187. Jin, X.C.; Shah, S.N.; Truax, J.A.; Roegiers, J.C. A Practical Petrophysical Approach for Brittleness Prediction from Porosity and Sonic Logging in Shale Reservoirs. In Proceedings of the 2014 SPE Annual Technical Conference and Exhibition, Amsterdam, The Netherlands, 27–29 October 2014.
188. Wang, F.P.; Gale, J.F. Screening criteria for shale-gas systems. *Gulf Coast Assoc. Geol. Soc. Trans.* **2009**, *59*, 779–793.
189. Jin, X.C.; Shah, S.N.; Roegiers, J.C.; Zhang, B. An integrated petrophysics and geomechanics approach for fracability evaluation in shale reservoirs. *SPE J.* **2015**, *20*, 518–526. [[CrossRef](#)]
190. Bishop, A.W. Progressive failure with special reference to the mechanism causing it. *Proc. Geotech. Conf.* **1967**, *2*, 142–150.
191. Andreev, G.E. *Brittle Failure of Rock Materials: Test Results and Constitutive Models*; A.A. Balkema: Rotterdam, The Netherlands, 1995; p. 446.
192. Luan, X.Y.; Di, B.R.; Wei, J.X.; Li, X.Y.; Qian, K.; Xie, J.Y.; Ding, P.B. Laboratory Measurements of brittleness anisotropy in synthetic shale with different cementation. In Proceedings of the 2014 SEG Annual Meeting, Denver, CO, USA, 26–31 October 2014; pp. 3005–3009.
193. Munoz, H.; Taheri, A.; Chanda, E.K. Fracture energy-based brittleness index development and brittleness quantification by pre-peak strength parameters in rock uniaxial compression. *Rock Mech. Rock Eng.* **2016**, *49*, 4587–4606. [[CrossRef](#)]
194. Ai, C.; Zhang, J.; Li, Y.W.; Zeng, J.; Yang, X.L.; Wang, J.G. Estimation criteria for rock brittleness based on energy analysis during the rupturing process. *Rock Mech. Rock Eng.* **2016**, *49*, 4681–5698. [[CrossRef](#)]
195. Yang, Y.; Sone, H.; Hows, A.; Zoback, M.D. Comparison of Brittleness Indices in Organic-rich Shale Formations. In Proceedings of the 47th US Rock Mechanics/Geomechanics Symposium, San Francisco, CA, USA, 23–26 June 2013.
196. Qian, K.R.; Zhang, F.; Li, X.Y. A rock physics model for estimating elastic properties of organic shales. In Proceedings of the 76th EAGE Conference and Exhibition, Amsterdam, The Netherlands, 16–19 June 2014.
197. Qian, K.R.; Zhang, F.; Chen, S.Q.; Li, X.Y.; Zhang, H. A rock physics model for analysis of anisotropic parameters in a shale reservoir in Southwest China. *J. Geophys. Eng.* **2016**, *13*, 19–34. [[CrossRef](#)]
198. Zhang, Y.X.; He, J.M.; Li, X.; Lin, C. Experimental study on the supercritical CO₂ fracturing of shale considering anisotropic effects. *J. Pet. Sci. Eng.* **2019**, *173*, 932–940. [[CrossRef](#)]
199. Chong, Z.H.; Yao, Q.L.; Li, X.H. Experimental investigation of fracture propagation behavior induced by hydraulic fracturing in anisotropic shale cores. *Energies* **2019**, *12*, 976. [[CrossRef](#)]
200. Hadei, M.R.; Veiskarami, A.; Sherizadeh, T.; Sunkpal, M. A laboratory investigation of the effect of bedding plane inclination angle on hydro-fracturing breakdown pressure in stratified rocks. In Proceedings of the 53rd U.S. Rock Mechanics/Geomechanics Symposium, New York, NY, USA, 23–26 June 2019.
201. Asadpoure, A.; Mohammadi, S. Developing New Enrichment Functions for Crack Simulation in Orthotropic Media by the Extended Finite Element Method. *Int. J. Numer. Methods Eng.* **2007**, *69*, 2150–2172. [[CrossRef](#)]
202. Wang, X.L.; Shi, F.; Liu, H.; Wu, H.A. Numerical Simulation of Hydraulic Fracturing in Orthotropic Formation Based on the Extended Finite Element Method. *J. Nat. Gas Sci. Eng.* **2016**, *33*, 56–69. [[CrossRef](#)]
203. Warpinski, N.R.; Teufel, L.W. Influence of geologic discontinuities on hydraulic fracture propagation. *J. Pet. Technol.* **1987**, *39*, 209–220. [[CrossRef](#)]

204. Zhou, J.; Chen, M.; Jin, Y.; Zhang, G.Q. Analysis of fracture propagation behavior and fracture geometry using a triaxial fracturing system in naturally fractured reservoirs. *Int. J. Rock Mech. Min. Sci.* **2008**, *45*, 1143–1152. [[CrossRef](#)]
205. Gu, H.R.; Weng, X.W. Criterion for fractures crossing frictional interfaces at non-orthogonal angles. In *Rock Mechanics Symposium: Proceedings of the 44th US Rock Mechanics Symposium and 5th US–Canada Rock Mechanics Symposium, Salt Lake City, UT, USA, 27–30 June 2010*; American Rock Mechanics Association: Alexandria, VA, USA, 2010.
206. Gu, H.R.; Weng, X.W.; Lund, J.B.; Mack, G.M.; Ganguly, U.; Suarez-Rivera, R. Hydraulic fracture crossing natural fracture at nonorthogonal angles: A criterion and its validation applications. *SPE Prod. Oper.* **2012**, *27*, 20–26. [[CrossRef](#)]
207. Blanton, T.L. Propagation of hydraulically and dynamically induced fractures in naturally fractured reservoirs. In *Proceedings of the SPE/DOE Unconventional Gas Technology Symposium, Louisville, KY, USA, 18–21 May 1986*.
208. Renshaw, C.E.; Pollard, D.D. An experimentally verified criterion for propagation across unbonded frictional interfaces in brittle, linear elastic materials. *Int. J. Rock Mech. Min. Sci.* **1995**, *32*, 237–249. [[CrossRef](#)]
209. Sarmadivaleh, M.; Rasouli, V. Modified Reinshaw & Pollard criteria for a non-orthogonal cohesive natural interface intersected by an induced fracture. *Rock Mech. Rock Eng.* **2013**, *47*, 2107–2115.
210. Wang, J.; Xie, H.P.; Li, C.B. Anisotropic failure behaviour and breakdown pressure interpretation of hydraulic fracturing experiments on shale. *Int. J. Rock Mech. Min. Sci.* **2021**, *142*, 104748. [[CrossRef](#)]
211. Thiercelin, M.; Roegiers, J.C.; Boone, T.J.; Ingraffea, A.R. An investigation of the material parameters that govern the behavior of fractures approaching rock interfaces. In *Proceedings of the 6th International Congress of Rock Mechanics, Montreal, Canada, 30 August–3 September 1987*.
212. Zou, Y.S.; Ma, X.F.; Zhang, S.C.; Zhou, T.; Li, H. Numerical investigation into the influence of bedding plane on hydraulic fracture network propagation in shale formations. *Rock Mech. Rock Eng.* **2016**, *49*, 3597–3614.
213. Huang, B.X.; Liu, J.W. Experimental investigation of the effect of bedding planes on hydraulic fracturing under true triaxial stress. *Rock Mech. Rock Eng.* **2017**, *50*, 2627–2643. [[CrossRef](#)]
214. Tan, P.; Jin, Y.; Han, K.; Hou, B.; Chen, M.; Guo, X.F.; Gao, J. Analysis of hydraulic fracture initiation and vertical propagation behavior in laminated shale formation. *Fuel* **2017**, *206*, 482–493. [[CrossRef](#)]
215. Yin, P.F.; Yang, S.Q.; Gao, F.; Tian, W.L.; Zeng, W. Numerical investigation on hydraulic fracture propagation and multi-perforation fracturing for horizontal well in Longmaxi shale reservoir. *Theor. Appl. Fract. Mech.* **2023**, *125*, 103921. [[CrossRef](#)]
216. Cheng, W.; Jin, Y.; Chen, M.A.; Xu, T.; Zhang, Y.K.; Diao, C. A criterion for identifying hydraulic fractures crossing natural fractures in 3D space. *Pet. Explor. Dev.* **2014**, *41*, 371–376. [[CrossRef](#)]

Disclaimer/Publisher’s Note: The statements, opinions and data contained in all publications are solely those of the individual author(s) and contributor(s) and not of MDPI and/or the editor(s). MDPI and/or the editor(s) disclaim responsibility for any injury to people or property resulting from any ideas, methods, instructions or products referred to in the content.